Volume 53
DOE/DP/40200-241

LLE Review

Quarterly Report

October–December 1992

Laboratory for Laser Energetics
College of Engineering and Applied Science
University of Rochester
250 East River Road
Rochester, New York 14623-1299

Volume 53
DOE/DP/40200-245

LLE Review

Quarterly Report

Editor: D. D. Meyerhofer
(716) 275-0255

October–December 1992

Laboratory for Laser Energetics
College of Engineering and Applied Science
University of Rochester
250 East River Road
Rochester, New York 14623-1299

IN BRIEF

This volume of the LLE Review covers the three-month period October–December 1992. On 18 December, the OMEGA Laser Facility fired its last shot. It will be decommissioned during the next quarter to make room for the OMEGA Upgrade Laser Facility. This volume deals with two areas of interest for the OMEGA Upgrade, the development of advanced x-ray and neutron diagnostics and the development of long-pulse (>1-ns) laser sources. The first three articles discuss the development of time-dependent diagnostics. The development of an x-ray framing camera is described and measurements of the high-voltage pulse propagation in the camera are presented. Time-resolved and time-integrated neutron diagnostics for the OMEGA Upgrade are then discussed. Two schemes for the generation of >1-ns laser pulses are presented. Finally, the activities of the National Laser Users Facility and the GDL and OMEGA laser facilities are summarized.

Highlights of the research reported in this issue include

- The use of gated microchannel-plate detectors as high-speed framing cameras in laser-driven inertial-confinement fusion (ICF) experiments is described. Using an array of pinholes to image the target, detectors capable of generating up to 16 individual frames with ~90-ps resolution on a single laser shot are now in routine use.
- The picosecond propagation characteristics of a voltage pulse in a microchannel plate, used in x-ray framing cameras, were measured electro-optically.

The signal propagation velocity and dispersion, the line characteristic impedance, and the substrate dielectric constant were measured.

- A new streak-camera diagnostic for directly time-resolving the neutron burnwidth for ICF implosions is presented. The technique uses the *(n, p)* reaction in CH_2 to convert the neutron signal to a proton signal, which is proximity coupled to a CsI secondary electron emitter and subsequently recorded with a standard LLE large-format, x-ray streak camera. This technique can also be extended to high-speed, microchannel-plate framing cameras.
- The planned time-integrated nuclear diagnostics for the OMEGA Upgrade include "line-of-sight," single-hit detectors to measure the ion temperature and activation diagnostics coupled with rapid-extraction mechanisms. The longest-path ion-temperature diagnostic will be housed in a separate building outside the OMEGA Upgrade target chamber.
- Pulse-width control of laser oscillators through the use of intracavity, Fabry-Perot etalons is described. Pulses of 7-ns duration with no temporal modulation have been generated. The experimental measurements are in good agreement with the simple theory presented.
- The generation of long laser pulses (>1 ns) with arbitrary temporal shapes using spatial masking is described. An initially chirped pulse is spectrally dispersed within a grating pair and a binary mask is used to generate long pulses with short rise times.

CONTENTS

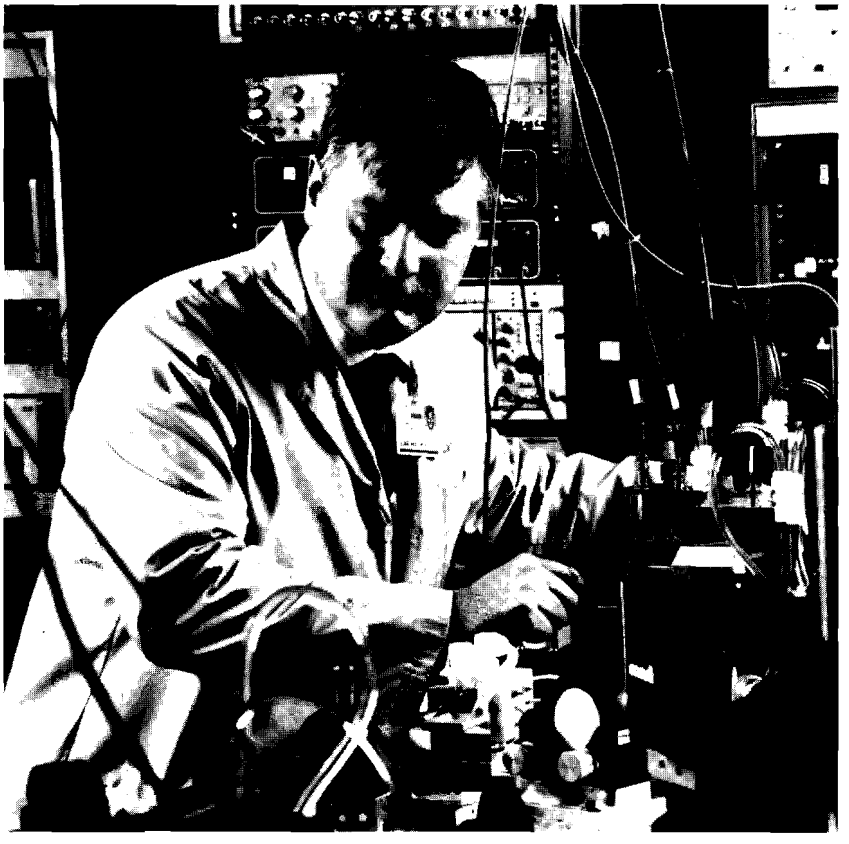

Dr. Mark Skeldon, Scientist, is shown adjusting an intracavity Fabry-Perot etalon, which is used to produce up to 7-ns laser pulses from a regenerative amplifier.

Section 1
ADVANCED TECHNOLOGY DEVELOPMENTS

1.A High-Speed, Gated X-Ray Imaging for ICF Target Experiments

The development of high-speed, gated x-ray imaging is of continuing interest in laser-driven, inertial-confinement fusion (ICF). High-gain ICF schemes require that the fuel capsule be compressed to high densities while maintaining a high degree of symmetry. Typical in-flight shell velocities during capsule implosions are in excess of 10^7 cm/s; so in order to maintain a spatial resolution of 10 μm or less with minimal motional blurring, x-ray gate times less than 100 ps are required. In this article data recorded using existing framing cameras with 90-ps time resolution are presented. This design has been further advanced to develop an even faster camera we believe is capable of producing multiframe x-ray images with sub-40-ps time resolution.

A number of framing-camera schemes have been proposed for producing high-speed gating of x rays.[1–5] However, the detector now used most widely for diagnosing laser-driven implosions, both on the OMEGA laser system at the University of Rochester's Laboratory for Laser Energetics (LLE) and on the NOVA laser at Lawrence Livermore National Laboratory (LLNL), is based on the high-speed gating of a proximity-focused microchannel-plate (MCP) device. Much of the work described here results from a collaboration between LLE and LLNL. Figure 53.1 shows a schematic of such a device. An incident x-ray image or spectrum is converted to a photoelectron replica by a gold photocathode coated onto the front of the MCP. These photoelectrons are directed down the channels of the MCP and amplified only when a voltage is applied. The amplified image is then proximity focused onto a phosphor screen on a fiber-optic faceplate

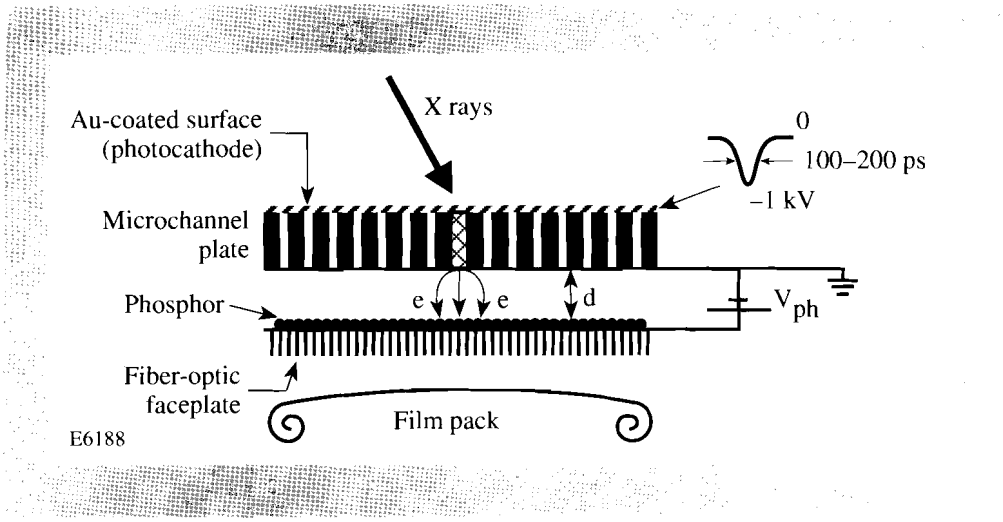

Fig. 53.1
Schematic of a microchannel plate x-ray camera. Electrons are multiplied through the MCP by voltage V_c and are then accelerated onto the phosphor by voltage V_{ph}.

and then recorded either on film or a CCD camera behind the phosphor. In our detectors the phosphor is typically 0.5 mm behind the MCP and is biased to +3 kV. For gating applications, the gold coatings on the front and back of the MCP are made to form a microstrip line, the glass of the MCP being the dielectric. A high-voltage pulse propagated along this microstrip will then result in localized gating of the MCP wherever the voltage is applied. The extreme nonlinearity of electron gain in an MCP as a function of applied voltage (the gain is proportional to V^9 for a $L/D = 40$ MCP, where L/D is the ratio of a channel's length to its diameter) means that the resultant "shutter time" is significantly less than the width of the applied voltage pulse.

The high-voltage, high-speed pulses needed to gate the MCP's are produced by the reverse breakdown of avalanche diodes.[6,7] Similar pulses can be obtained by using photoconductive switches,[8] but the need for a synchronized ultrafast laser pulse to trigger them makes them less practical for use on current ICF experiments.

The need to be able to project high-magnification (>10×) images of imploding targets onto the detector sets a minimum width for the microstrip line coated on the MCP and hence a maximum value for its impedance. The lower the impedance the higher the power-output requirements from the high-voltage pulser. Multiple microstrip lines coated on a single detector create an even greater power requirement. Early designs attempted to reduce these gating power requirements by coating four open-ended strips onto the MCP and using the open circuit reflection to double the input pulse.[9] However, this scheme has the disadvantage that the voltage doubling only occurs over a distance equivalent to half the voltage pulse width from the open circuit and is nonuniform for any pulse shape other than a square top.

An arrangement that has been widely used to date is that of a single-meander or serpentine microstrip line as shown in Fig. 53.2. The 6-mm-wide, 12.5-Ω line is fed by a 1-kv, 150-ps pulse generated by a pair of synchronized avalanche-diode pulsers. A pinhole array projects 14 separate x-ray images of the target onto the channel plate. Each image is gated on and off in turn as the voltage pulse

propagates along the microstrip. The interframe time is ~50 ps and is obtained simply from the distance between images (7.5 mm) divided by the electrical pulse propagation velocity (1.52 cm/100 ps). The shutter time of this instrument has been measured to be ~90 ps by illuminating the whole MCP with a non-imaged 20-ps x-ray burst from a short-pulse NOVA shot and measuring the width of the resultant gated image. The advantages of the meander microstrip arrangement are that the single strip requires much less power to drive than three separate strips and that it is a simple system with fixed interframe times. However, dispersion and peak voltage loss are worse with the longer strip[10] (the dc resistance of the strip is ~2 Ω), and the presence of slight voltage reflections from the corners make flat-fielding difficult. The total time delay between the first and last image on this device is ~650 ps, which is an ideal window for implosions on the 600- to 700-ps OMEGA laser, but may not be adequate for laser systems with longer pulses.

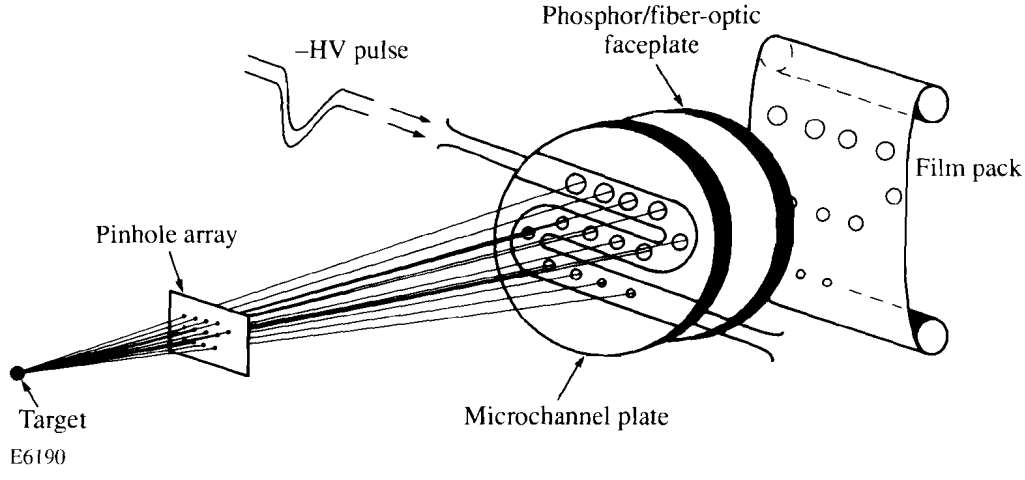

Fig. 53.2
Multiframe imaging x-ray framing camera based on a single-meander microstrip design.

Experimental Results

Figure 53.3 shows an example of the data recorded from the implosion of a deuterium-filled glass shell of 240-μm diam with 5-μm wall thickness directly driven by the OMEGA laser. The diagnostic was filtered by 25 μm of beryllium providing sensitivity in the spectral region above 1 keV. The initial images in Fig. 53.3 show x-ray emission from the glass shell, heated by the laser irradiation. As time progresses the shell begins to implode and the ring of emission becomes smaller. By the eighth or ninth frame, core emission from the center of the target becomes visible and begins to dominate as the implosion continues.

The success of ICF depends on the ability to maintain a high level of drive uniformity throughout the implosion. Perturbations seeded by either target or

irradiation nonuniformities may grow during the implosion with potentially catastrophic effects on capsule performance. One of the main applications of gated imaging is that it allows us a means of checking the accuracy of hydrocode predictions. This is achieved by comparing time-resolved measurements of the effect of intentionally applied perturbations with those predicted by simulations. One of the simplest perturbations to apply to an imploding target is that corresponding to the Legendre $\ell = 1$ mode. This can be generated by driving one side of the capsule harder than the other. An experiment in which a framing camera was used to monitor the development of an intentionally imposed $\ell = 1$ mode is described in Ref. 11.

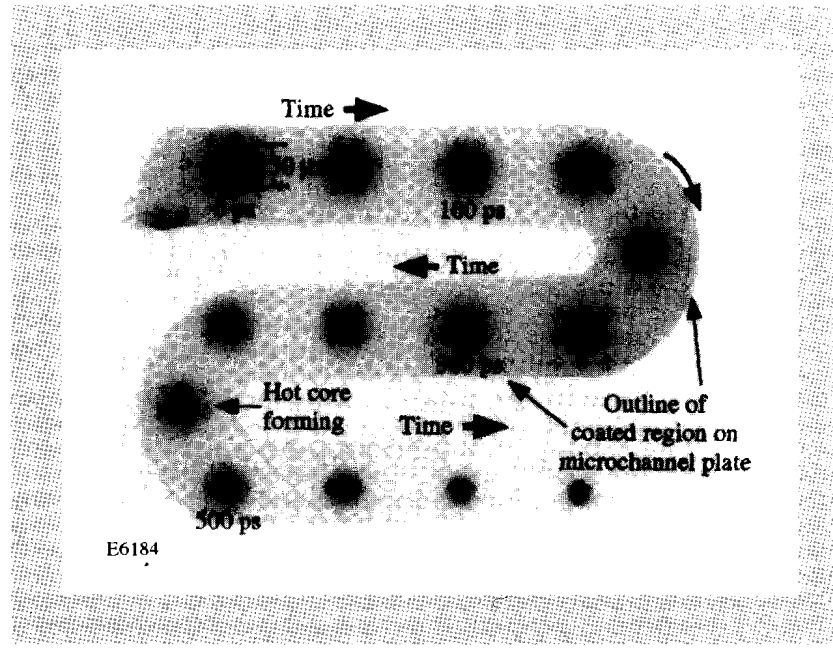

Fig. 53.3
Slightly overexposed image from the multiframe camera showing the implosion of a glass microballoon. The overexposure allows the outline of the coated region of the microchannel plate to be seen.

A slightly more complex perturbation, which demonstrates the usefulness of gated imaging rather well, is the imposition of an $\ell = 3$ mode on the capsule. Figure 53.4 shows the arrangement of OMEGA beams on target, as seen from one of our serpentine framing cameras. For the purposes of this experiment, the beams were split into four horizontal groups, labeled A to D from top to bottom of the target. The perturbation was applied by increasing the incident energy in group A while decreasing it in groups B and D. This was predicted to put most of the perturbation into ℓ-modes 1 and 3. The raw images from one of the shots in this experimental series are shown in Fig. 53.5. In this case a distortion of the limb becomes noticeable by the second frame and continues to grow throughout the implosion. Emission from the core is visible by the eighth frame. It is somewhat off-center by this point as a result of the $\ell = 1$ component of the perturbation, and as the implosion progresses, it moves off even further. The shell distortion can be seen more clearly in Fig. 53.6, in which an enlarged view of four of the images is shown together with an overlay denoting the original shape and size of the target. The magnitude and growth rate of the $\ell = 3$ perturbation on a spherical surface are best seen by replotting the images as a series of radius-versus-azimuthal-angle images, as in Fig. 53.7. Here, the growing distortion on

the imploding shell can be seen more clearly, as can the offset and position of the imploded core. (In this type of plot, a centralized undistorted core would be seen as a bright band across the bottom of the image.) Two-dimensional simulations of this experiment were carried out with *ORCHID* using experimentally measured values for the initial perturbation. Comparisons of experimental and code results are shown in Fig. 53.8, in which we have plotted the growths of the Legendre coefficients of the $\ell = 1$ and $\ell = 3$ modes as a function of time. In both cases there is good agreement between experiment and simulation for both the size and growth rate of the individual modes.

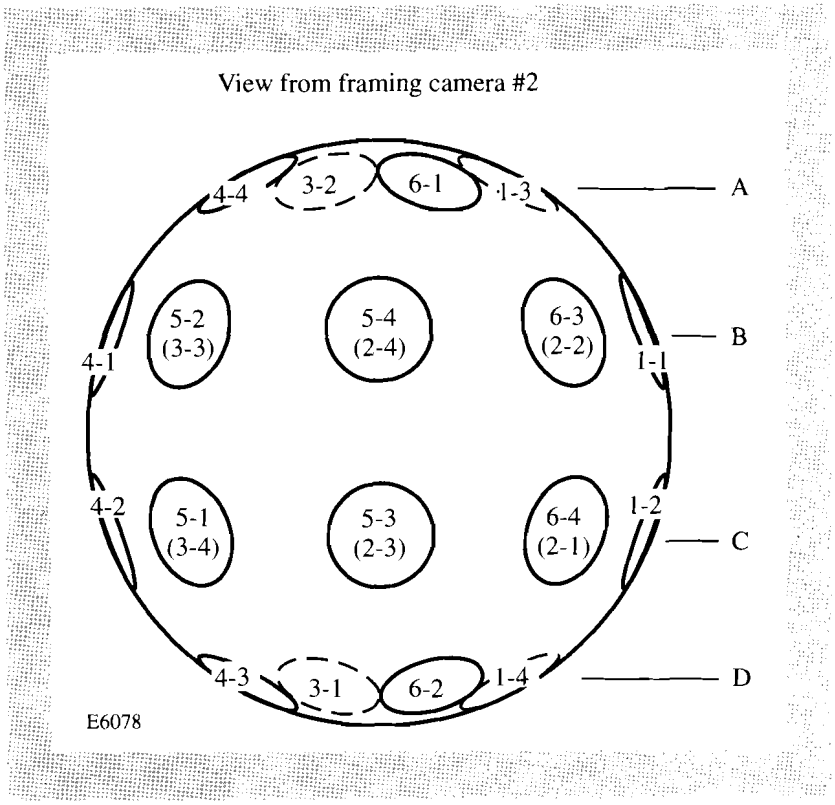

Fig. 53.4
Diagram showing the on-target positions of the centers of the 24 beams of OMEGA as seen by the framing camera. The dashed lines and parentheses denote beams obscured by the target.

The two experiments referred to in the preceding sections both imposed long-wavelength nonuniformities, which are typical of those expected from laser power-imbalance considerations, to drive a perturbation on a uniform (for long-wavelength modes) imploding sphere. In a recent experiment,[12] Glendinning and co-workers reported on an experiment in which a uniform laser beam was used to accelerate a mass-modulated planar foil. The diagnostic used was similar to the one described in Fig. 53.2, but since the drive laser was ~3 ns in length, four separately driven microstrips were used to provide an adequate time window. The Rayleigh-Taylor growth in both the linear and nonlinear phases of a range of single-mode perturbations from 20 μm to 100 μm was measured and compared to two-dimensional code simulations.

Higher-Speed Gating

There is a continuing need for even faster gating than the 90-ps frame times available on the current cameras. Unfortunately, because of electron transit-time

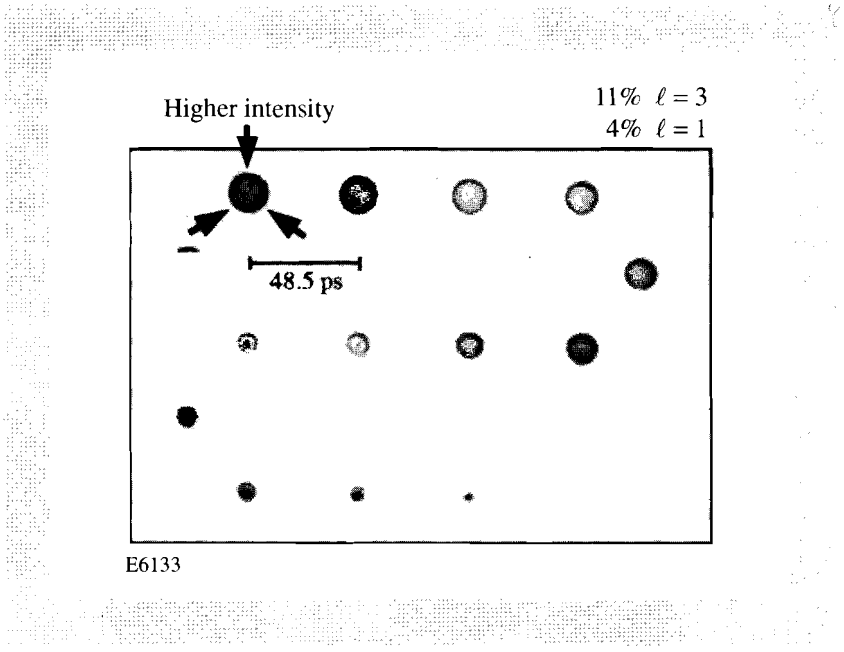

Fig. 53.5
Framing-camera image showing implosion of glass microballoon with intentionally applied drive nonuniformities in the $\ell = 1$ and $\ell = 3$ modes.

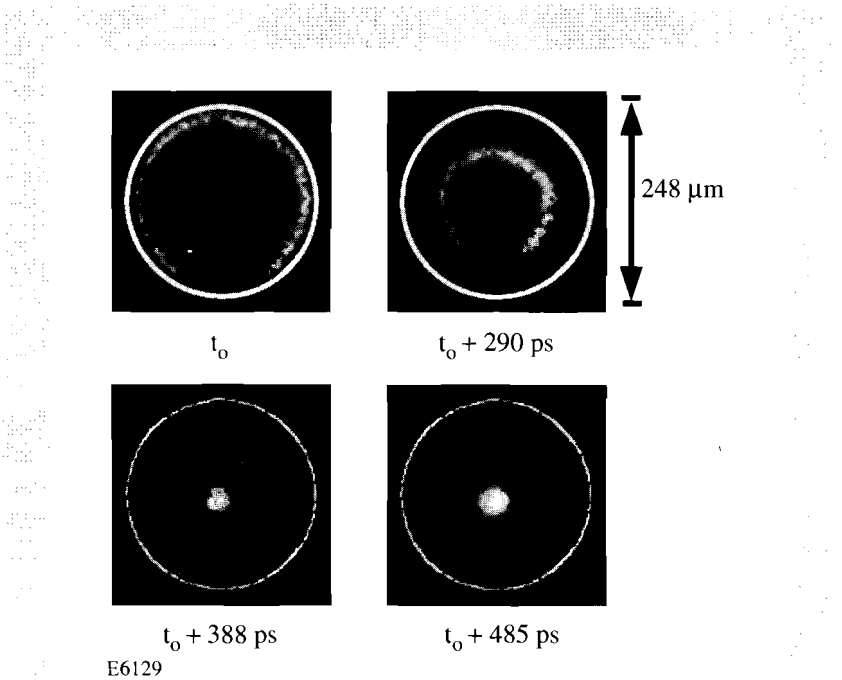

Fig. 53.6
Enlargement of four of the frames from Fig. 53.5. The white circle shows the original position of the target.

effects, this cannot be achieved by merely sending a shorter voltage pulse into the MCP microstrip on the current cameras. When the electron transit time through the MCP is small compared to the duration of the voltage pulse, the gate time depends simply on the voltage pulse width and is shortened because of the scaling of MCP gain with applied voltage. (This factor is approximately 1/3 for a Gaussian voltage pulse in an $L/D = 40$ MCP, where the gain is proportional

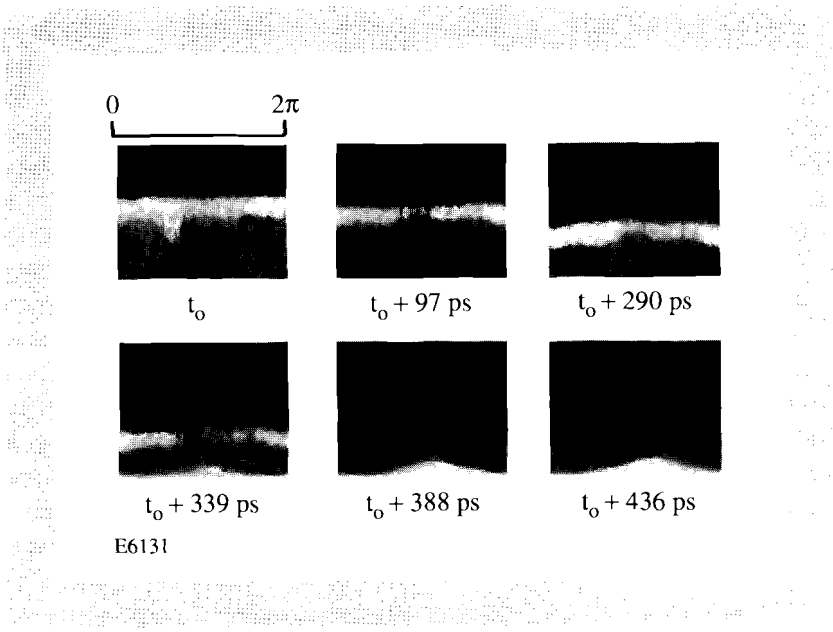

Fig. 53.7
Selection of individual frames from Fig. 53.5 replotted in terms of radius versus azimuthal angle.

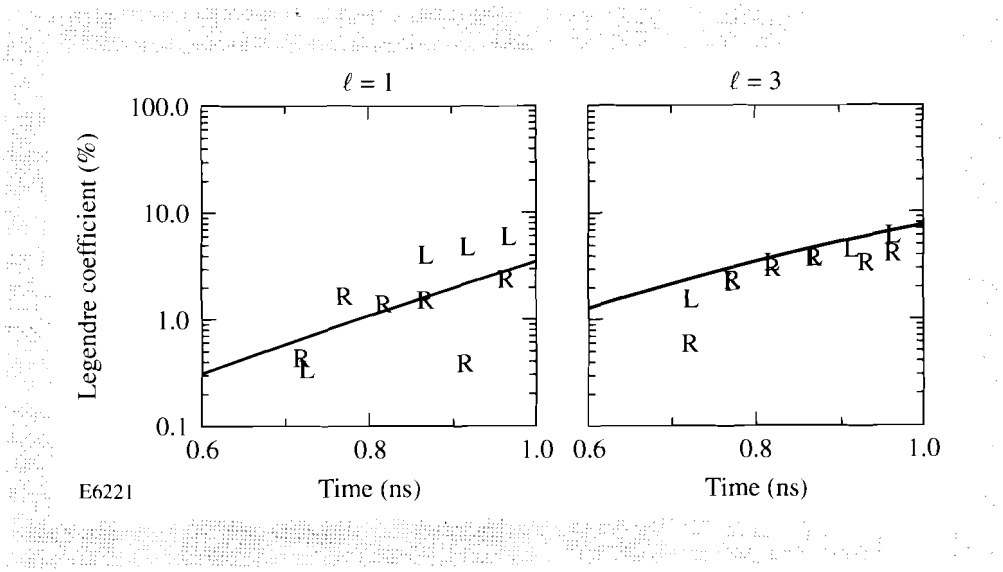

Fig. 53.8
Comparison of experimental data with an *ORCHID* simulation (solid line) showing the growth of the Legendre $\ell = 1$ and $\ell = 3$ modes. L and R refer to the left and right hemispheres of individual images.

to V[9].)[7] However, when the voltage pulse width becomes comparable to, or less than the electron transit time (which is the case for all our detectors), it is no longer possible to extract all of the secondary photoelectrons during the applied voltage pulse, and a time-dependent model for the electron gain has to be used.[7,13] This model indicates that the minimum achievable gate time then becomes a fixed fraction of the transit time, typically between 1/2 and 1/3. The electron transit time can be expressed as $T = (m/\mathrm{eV})^{1/2} L(L/D)^{1/2}$, where m is the electron mass. This equation shows that faster gating should be achievable by using higher voltages, decreasing the MCP thickness, or by reducing the aspect ratio of the MCP pores. However, channel-saturation effects[7] restrict the maximum voltage that can be usefully applied to ~1 kV for the $L/D = 40$ plates. At this voltage the transit time is 247 ps for the 0.5-mm-thick plates used in the

serpentine cameras and the fastest gate time is around 90 ps. Reductions in the MCP thickness and channel aspect ratio have, however, proven more fruitful. In off-line tests, gate times of 50 ps have been recorded using thinner (250-μm thickness) plates[14] and measurements with 65-ps duration voltage pulses on 200-μm thickness, reduced aspect-ratio (L/D = 20) plates indicated that sub-40-ps gating was achieved.[15,16] In both these cases, very narrow (typically 1.5- to 2-mm) and hence, high impedance (15- to 25-Ω) microstrips had to be used to maintain sufficient voltage on the detector. Off-line measurements of the voltage-pulse duration are described in the following article.

We have now been able to construct a full-size detector using a 200-μm-thick, L/D = 20 microchannel plate. In order to maintain the ~6-mm-wide microstrip format used in the current generation of cameras (necessary for high-magnification imaging of large targets), we have had to use a 6-Ω line, which places severe demands on the output of the pulser. It is also necessary to use a multistrip (four-strip) format as it would not be possible to propagate the high-voltage, 60- to 80-ps pulse along the full length of the long meander strip. The pulse is fed onto the strip through a 50- to 6-Ω tapered stripline.[16] The high-voltage pulse used to gate the device was generated using an adaptation of the avalanche-diode circuit used for the serpentine cameras and is shown in Fig. 53.9. The main changes to the circuit are that two diodes are now used to produce a higher output voltage and that the diodes are now used in a shunt format as opposed to the series configuration used in the earlier pulsers.[17] The main advantage of the shunt configuration is that any precursor to the main gating pulse will be of opposite polarity to it, and that it also helps to generate a faster rise time on the pulse itself. The pulser generates a 2700-V, 80-ps negative pulse into 50 Ω, which reduces to 750–800 V by the time it reaches the microstrip on the MCP.[16] Since the output from an L/D = 20 microchannel plate is much lower than for an L/D = 40 plate (gain is proportional to $V^{4.5}$ instead of V^9), an additional L/D = 40 plate was placed behind the gated plate and run with dc bias to boost the total output from the detector.

To test the temporal resolution of the device, 202-nm-wavelength pulses from a 3-ps, frequency-tripled dye laser were focused through an expanding-lens/cylindrical focusing-lens pair to produce a uniform line focus along the length of an individual microstrip.[15] Although the photoelectron energy distribution produced from the UV light is different from that produced by x rays, it is assumed that the gate time, which should be dominated by secondary electron processes, will be the same in both cases. The pulse to the MCP was triggered by a low-jitter system capable of less than 30-ps jitter. Output images from the device were recorded on a Photometrics CCD camera lens coupled to the phosphor. The temporal response of the gated detector is measured from the spatial extent of the output image along the microstrip, divided by the electrical pulse-propagation velocity as shown in Fig. 53.10.

The gated plate was operated with a variety of reverse-bias voltages. The voltage applied to the dc plate could be adjusted to maintain a suitable light-output level at the phosphor. The reverse bias was applied to reduce the effective temporal width of the electrical pulse. Figure 53.11 shows a CCD image from a

pulse in which a 300-V reverse bias was applied to the plate. The dc plate voltage was 700 V and the phosphor-acceleration voltage was 3.3 kV. Also in Fig. 53.11 we have displayed a lineout through the image; the time scale has been corrected for the measured electrical-pulse-propagation velocity of 1.52 cm/100 ps. This shows a somewhat asymmetric pulse with a slightly slower rise than fall time and a FWHM of 37 ps. No noticeable change in the gate width was observed when the reverse bias was increased to 425 V, but a decrease in reverse bias to 200 V caused a slight increase in the gate width to 44 ps.

Summary

X-ray framing cameras, based on the high-speed gating of microchannel plates, are now in routine use on laser-driven ICF experiments. Devices capable of generating up to 16 frames with ~90-ps temporal resolution have been used to diagnose the development of intentionally applied perturbations in laser-driven targets. New devices, based on thinner, reduced-aspect-ratio MCP's, are now capable of similar performance with 40-ps resolution or better.

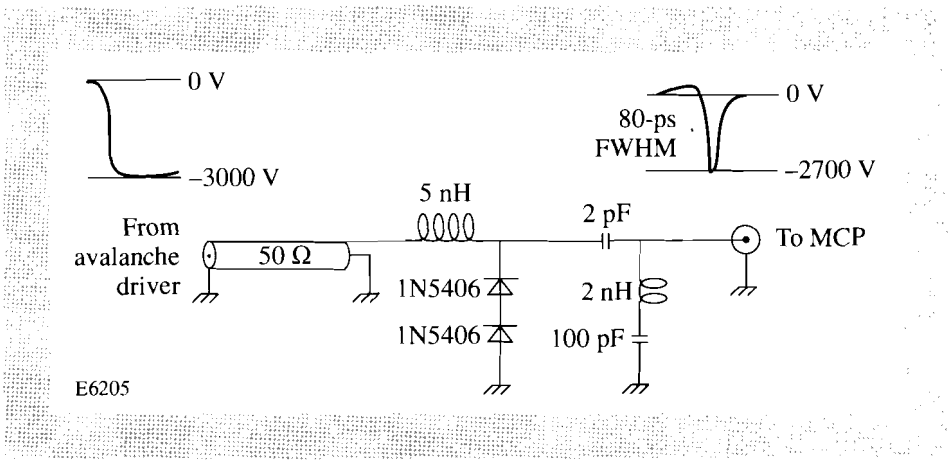

Fig. 53.9
Schematic showing the multikilovolt pulser used to gate the high-speed camera.

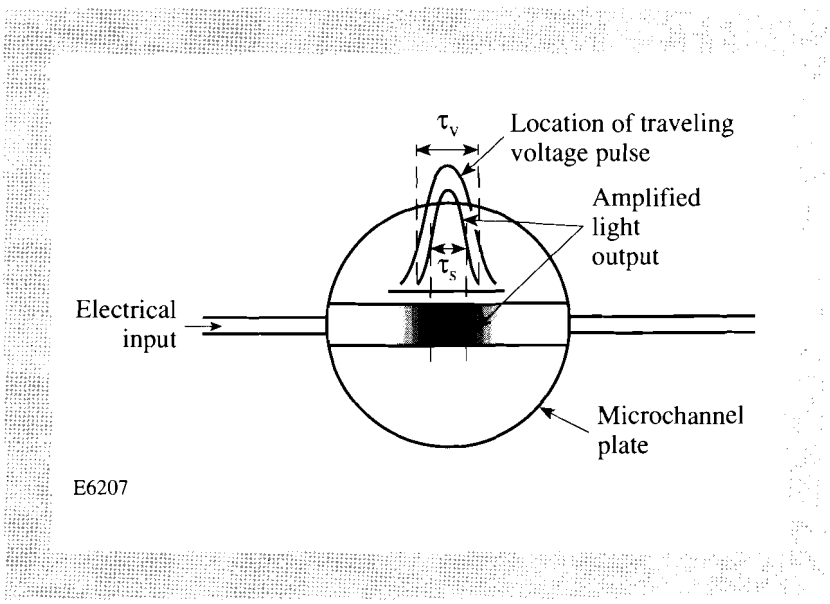

Fig. 53.10
Schematic showing how the output from the gated detector is used to calculate the FWHM of the frame time.

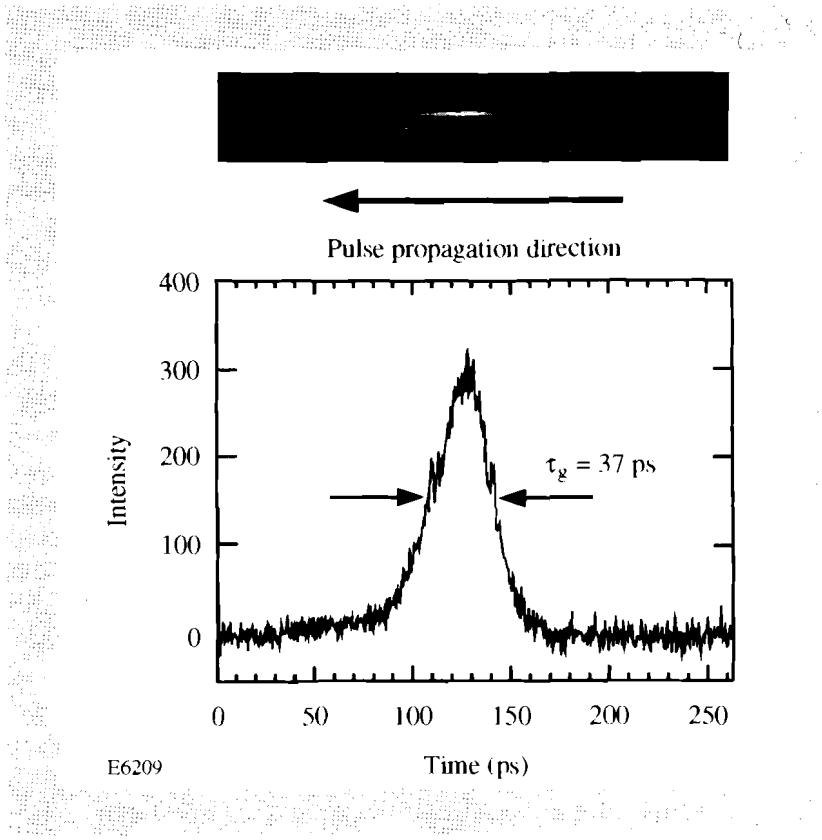

Fig. 53.11
Image of line focus recorded by the gated camera. The lineout shows that the FWHM of the gate is 37 ps.

ACKNOWLEDGMENT

This work was supported by the U.S. Department of Energy Office of Inertial Confinement Fusion under Cooperative Agreement No. DE-FC03-92SF19460, the University of Rochester, and the New York State Energy Research and Development Authority. The support of DOE does not constitute an endorsement by DOE of the views expressed in this article.

REFERENCES

1. N. Finn, T. A. Hall, and E. McGoldrick, Appl. Phys. Lett. **46**, 731 (1985).
2. W. Sibbett, M. R. Baggs, and H. Niu, in *15th International Congress on High Speed Photography and Photonics* (SPIE, Bellingham, WA, 1982), Vol. 348, p. 267.
3. R. Kalibjian and S. W. Thomas, Rev. Sci. Instrum. **54**, 1626 (1983).
4. J. D. Hares, in *X Rays from Laser Plasmas* (SPIE, Bellingham, WA, 1987), Vol. 831, p. 165.
5. D. G. Stearns *et al.*, Rev. Sci. Instrum. **57**, 2455 (1986).
6. I. V. Grekhov, A. F. Kardo-Sysoev, and S. V. Shenderei, Instrum. Exp. Tech. **24**, 967 (1981).
7. J. D. Kilkenny, Laser & Part. Beams **9**, 49 (1991).
8. D. H. Auston, in *High Speed Optical Techniques* (SPIE, Bellingham, WA, 1976), Vol. 94, p. 78; G. Mourou and W. Knox, Appl. Phys. Lett. **35**, 492 (1979).

9. D. K. Bradley, J. Delettrez, P. A. Jaanimagi, F. J. Marshall, C. P. Verdon, J. D. Kilkenny, and P. Bell, in *High Speed Photography, Videography, and Photonics VI* (SPIE, Bellingham, WA, 1988), Vol. 981, p. 176.

10. P. M. Bell, J. D. Kilkenny, G. Power, R. Bonner, and D. K. Bradley, in *Ultrahigh Speed and High Speed Photography, Photonics, and Videography '89* (SPIE, Bellingham, WA, 1989), Vol. 1155, p. 430.

11. P. W. McKenty, C. P. Verdon, S. Skupsky, R. L. McCrory, D. K. Bradley, W. Seka, and P. A. Jaanimagi, J. Appl. Phys. **68**, 5036 (1990).

12. S. G. Glendinning, Bull. Am. Phys. Soc. **36**, 2375 (1991).

13. E. H. Eberhardt, ITT Electro Optical Products Division Technical Note, No. 127 (1980).

14. P. M. Bell *et al.*, in *Ultrahigh Speed and High Speed Photography, Photonics, and Videography '89* (SPIE, Bellingham, WA, 1989), Vol. 1155, p. 415.

15. P. M. Bell *et al.*, in *Ultrahigh- and High-Speed Photography, Videography, Photonics, and Velocimetry '90* (SPIE, Bellingham, WA, 1990), Vol. 1346, p. 456.

16. J. D. Kilkenny, P. M. Bell, B. A. Hammel, R. Hanks, O. Landen, T. McEwan, D. S. Montgomery, R. E. Turner, J. D. Wiedwald, and D. K. Bradley, in *19th International Congress on High-Speed Photography and Photonics* (SPIE, Bellingham, WA, 1990), Vol. 1358, p. 117.

17. T. E. McEwan and R. L. Hanks, in *Ultrahigh- and High-Speed Photography, Videography, Photonics, and Velocimetry '90* (SPIE, Bellingham, WA, 1990), Vol. 1346, p. 465.

1.B Characterization of Microchannel-Plate Detectors for High-Speed, Gated X-Ray Imaging by Electro-Optic Sampling

A widely used device for diagnosing laser-driven, inertial-confinement-fusion experiments is based on the high-speed, x-ray gating of a proximity-focused microchannel-plate (MCP) detector.[1] This device was described in article 1.A of this volume. The MCP is a nonhomogeneous air/glass dielectric medium that provides extremely high (nonlinear) electron gain. For gating applications, a microstrip line (see Fig. 53.1, article 1.A of this volume) is fabricated by coating a 1- to 6.55-mm-wide, 500-nm-thick Au/Cu center conductor on the front and a 500-nm-thick Au/Cu ground plane on the back of the MCP. A short (<100-ps) high-voltage pulse is propagated along this microstrip, resulting in a localized gating on the MCP wherever the voltage is applied (Fig. 53.12). Obviously, the exact knowledge of the pulse-propagation characteristics (e.g., propagation velocity, attenuation, bend-induced dispersion, etc.) is critical to the optimal design of the MCP x-ray detector and correct analysis of the obtained experimental data.

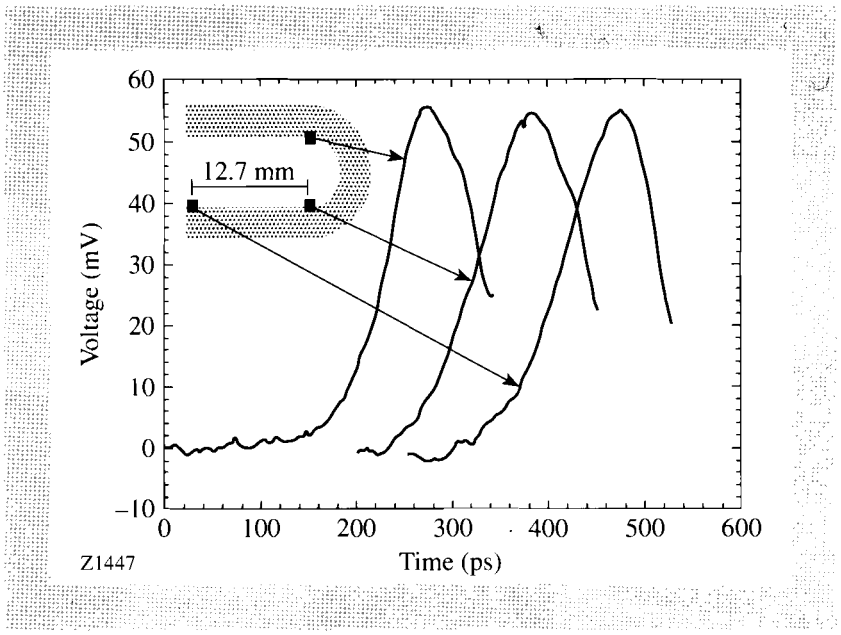

Fig. 53.12
Experimentally measured waveforms sampled before and after the pulse entered the MCP serpentine bend. The input pulse was ~100 ps wide.

In this article, we present a picosecond characterization of the MCP microstrip detector. Our measurements were performed using the electro-optic sampling system described in detail in Ref. 2. Briefly, a photoconductive switch was illuminated with ~140-fs-wide laser pulses (λ = 750 nm), produced by a commercial (Mira 900), mode-locked, Ti:Al_2O_3 laser. The switch was formed in a microstrip transmission-line configuration and was coupled to the MCP microstrip line. This arrangement produced 20- to 100-ps-wide electrical pulses, which were launched onto the MCP transmission line. The propagated pulses were *externally* sampled at different positions along the line with a $LiTaO_3$ finger probe positioned near the conductor edge.

We have found (see Fig. 53.12) that ~100-ps-wide pulses propagated along the microstrip serpentine transmission line without any significant attenuation or pulse distortion. On the other hand, shorter pulses exhibited substantial degradation, even before entering the first bend. Figure 53.13 shows the ~20-ps-wide waveforms sampled at intervals of 2.54 mm along the MCP detector. We observed that in this case the signal rise time increased as the waveform propagated along the line, indicating signal dispersion. Simultaneously, the peak voltage of the propagating pulses decreased.

The measured electrical transients allowed us to determine the signal arrival time, taken to be the midpoint of the rising edge. Based on our measurements, we calculated the signal-propagation velocity, which varied from 0.52 to 0.65 of the speed of light, depending on the line dimensions and MCP porosity. The propagation velocity, in turn, allowed us to determine the line-characteristic impedance and the relative dielectric constant, which was found to range from 2.46–4.08.

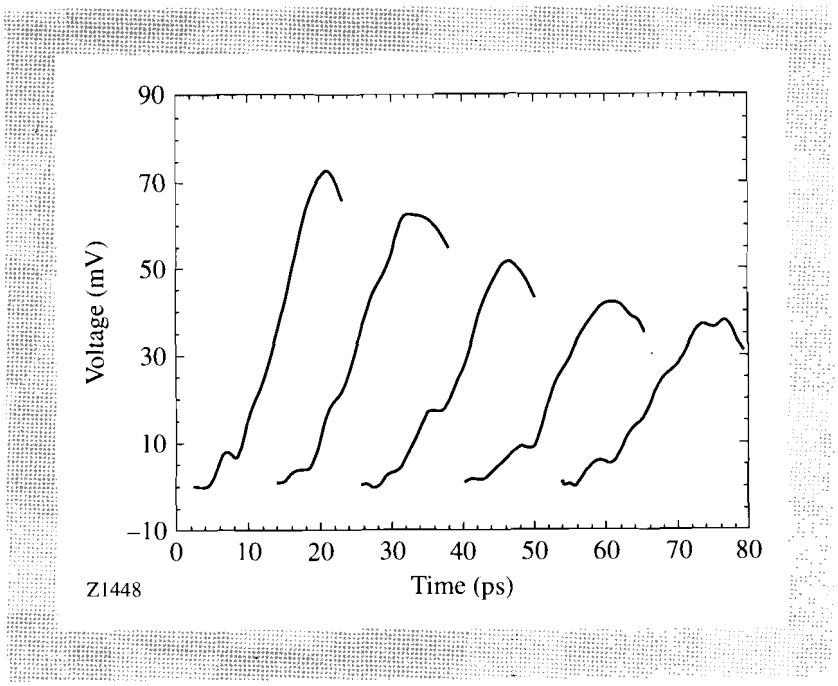

Fig. 53.13
Experimentally measured waveforms sampled every 2.54 mm. The input pulse was ~20 ps wide.

In conclusion, electro-optic sampling was applied, for the first time, in the characterization of MCP x-ray detectors, used in diagnosing laser-driven fusion implosions, both on the OMEGA laser system at LLE and on the NOVA laser at LLNL. We have shown that the transient characteristics of the MCP microstrip can be readily extracted from our waveform measurements, providing important information about the MCP detector operation. The described experiments also demonstrated the feasibility of very accurate time-domain characterization of millivolt-level picosecond signals propagating on very-low-impedance microstrips, such as those often found in GaAs microwave devices and Si-based superconducting digital circuits.

ACKNOWLEDGMENT

The work was supported by the University Research Initiative at the University of Rochester sponsored by the Army Research Office grant No. DAAL03-92-G-0112. This work was also supported by the U.S. Department of Energy Office of Inertial Confinement Fusion under Cooperative Agreement No. DE-FC03-92SF19460, the University of Rochester, and the New York State Energy Research and Development Authority. The support of DOE does not constitute an endorsement by DOE of the views expressed in this article.

REFERENCES

1. D. K. Bradley, P. M. Bell, J. D. Kilkenny, R. Hanks, O. Landen, P. A. Jaanimagi, P. W. McKenty, and C. P. Verdon, Rev. Sci. Instrum. **63**, 4813 (1992).
2. S. Alexandrou, R. Sobolewski, and T. Y. Hsiang, IEEE J. Quantum Electron. **28**, 2325 (1992).

1.C Neutron Streak- and Framing-Camera Diagnostics for ICF Implosions

High-fidelity, time-resolved measurements of the neutron flux from the implosion of DT- and/or DD-filled capsules have been a challenging problem for the international inertial-confinement-fusion (ICF) community. A measure of the neutron production rate can provide valuable information on the quality of the implosion, such as the confinement time of the plasma. A time-resolving neutron detector is generally used to measure the neutron-production rate since the neutron is the fusion product most likely to escape the burn region and the target without further interaction, thus preserving temporal information. The neutron energies are 14.1 MeV and 2.45 MeV for DT and DD fusion reactions, respectively, and typical fusion burnwidths are in the range of 100–300 ps. In this article we report on a new streak-camera diagnostic for directly time-resolving the neutron burnwidth for ICF implosions. The technique uses elastic scattering of the neutrons in CH_2 to convert the neutron signal to a recoil-proton signal, which is proximity coupled to a CsI secondary electron emitter and is subsequently recorded with a standard LLE large-format, x-ray streak camera. Baseline requirements for the neutron detector include the following: directly measured time resolution better than 20 ps; should be positionable to less than 5 cm from the capsule to minimize the transit time spread caused by the velocity distribution of the neutrons (this depends on the neutron source temperature); incorporate an optical or x-ray timing fiducial to establish burn time to within ±20 ps; should be capable of recording on the same shot the time histories of both the primary DD and the secondary DT neutrons (the secondary/primary yield ratio is typically 1%). Further, the instrument needs to be shielded from the background of γ rays, and thermalized and inelastically scattered neutrons originating from nearby diagnostics and the target chamber itself.

Three independent techniques have been used to measure the neutron burnwidth. The first is a neutron streak camera incorporating a UO_2 photocathode.[1–6] U^{238} has a fission cross-section of 1.1 b for 14.I-MeV neutrons, which is equivalent to a 1/e absorption length of 37 cm in UO_2. The cross section for 2.45-MeV neutrons is 0.55 b. The basis of this technique is the large number (>300) of secondary electrons generated in the UO_2 layer by the fission fragments.[7] These secondary electrons have an energy <20 eV and an energy spread FWHM <6 eV, which makes their detection amenable to standard streak-tube electron optics with a time resolution better than 20 ps. However, UO_2 photocathodes suffer from a lack of sensitivity. The photocathode thickness is typically 1–3 μm because of the small range of the fission fragments (<10 μm); therefore, the number of fission events/neutron is $<10^{-5}$. This has led to the proposal and/or development of some complex, large-area photocathode, streak-tube designs that can be positioned close to the neutron source.[1,2,6] These designs can be inefficient (by filtering for a narrow electron-energy spectrum) in collecting the numerous secondary electrons emitted from the UO_2 photocathode, as typically only a few electrons need to be recorded to unambiguously detect an event above the background. Recording 50–100 electrons per fission event only

serves to limit the dynamic range of the streak tube and does not enhance the sensitivity of the detector. Of relevance to this article is the improvement in the secondary electron spectrum when the UO_2 was overcoated with a thin layer of CsI.[6]

A second method for recording fusion burnwidths is to use a neutron-damaged GaAs photoconductor.[8] These small detectors trade off size and therefore sensitivity (active volume to absorb neutrons) for better time response. GaAs detectors ($1 \times 1 \times 3$ mm in size) mounted in a 50-Ω transmission line have demonstrated an impulse response of 60-ps FWHM, but when coupled to a 6-GHz oscilloscope, the time resolution degraded to 130 ps.

The third technique for measuring the neutron flux is to couple the output from a fast scintillator or other neutron-to-light converter to an optical streak camera. This type of detector is currently being used on the GEKKO XII laser facility at Osaka[9] and also on the NOVA laser facility at LLNL.[10] Advantages of these detectors are (1) the small size of the light converter allows it to be positioned <1 cm from the fusion capsule and (2) the streak camera can be placed at a distance from the neutron source where it can be effectively shielded from the radiation background. Coupling to the streak camera is via an optical-fiber bundle or an optical-telescope relay system. The main drawback for the technique is that the impulse response of the converter (which may not be accurately known) must be deconvolved from the signal. Time resolution appears to be limited to about 50 ps.

In this article we present a fourth method for measuring the neutron flux from ICF capsules. Our detector is a standard large-format, LLE x-ray streak tube with a photocathode consisting of a 2500-Å layer of CsI on a 12.7-μm Be foil, which is backed with a 1-mm-thick piece of polyethylene (CH_2, density 0.91 g/cm^3). With this streak camera we have successfully recorded the neutron flux from the implosion of a DT-filled glass microballoon yielding 3×10^{10} neutrons, at a photocathode-to-target distance of 30 cm (Fig. 53.14). The basis of this technique is the generation of recoil protons by elastic scattering of the neutrons in CH_2. Cross sections in hydrogen are 0.7 b for DT neutrons at 14.1 MeV and 2.6 b for DD neutrons at 2.45 MeV, which are equivalent to neutron l/e absorption lengths in CH_2 of 18.3 cm and 4.9 cm, respectively. The recoil protons are forward directed and upon traversing the CsI will lose some of their energy to the electrons in the solid, which in turn generate low-energy secondary electrons. The energy spectrum of the secondary electrons is a characteristic of the photocathode material and not of the energy nor type of the primary excitation source. Therefore, the streak tube operation is identical to that for recording x-ray signals. The Be foil is simply a conductive substrate for the CsI layer, and a different metal foil may be used to moderate or filter the proton energy spectrum.

In the remaining sections of this article we present calculations of the impulse response of the neutron streak camera, followed by a discussion of the experimental results. Finally, we describe a proposal to apply the recoil-proton, radiator photocathode technique to the high-speed framing cameras described in the previous articles.

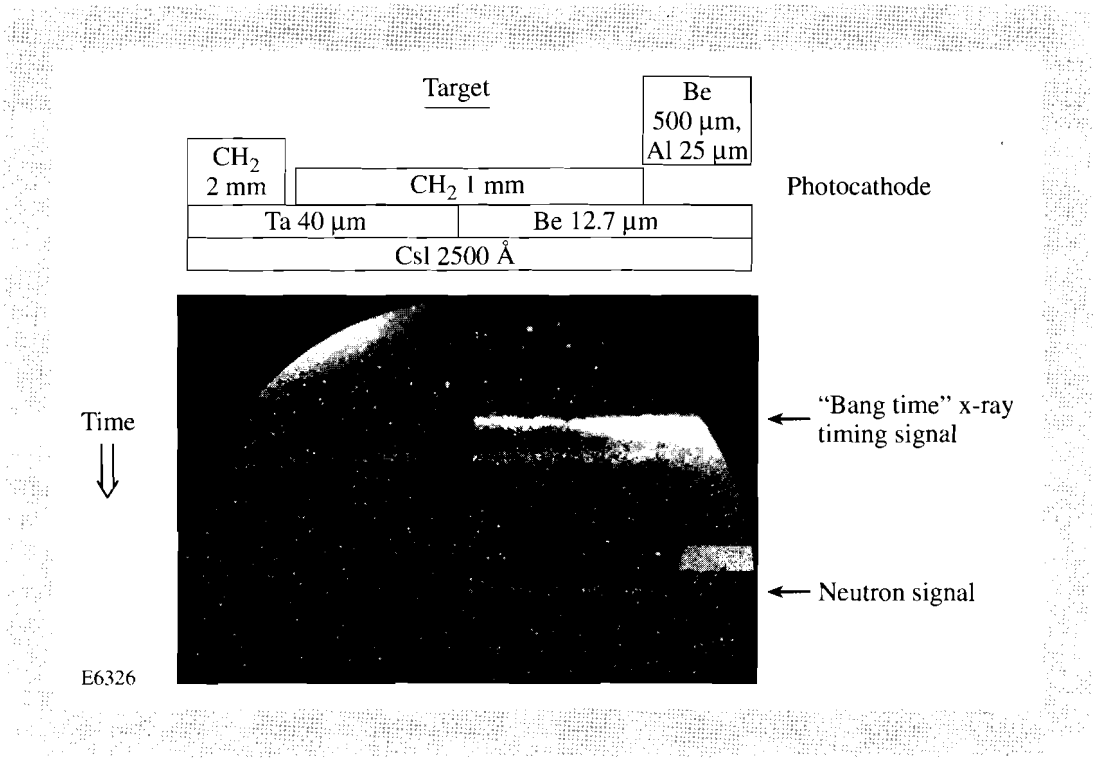

Fig. 53.14
Neutron streak-camera recording of the x-ray and 14.1-MeV neutron signals from the implosion of a DT-filled glass microballoon. Photocathode-to-target distance was 30 cm and the yield was 4×10^{10}. The structure of the photocathode is also detailed. The small rectangle on the right-hand side is caused by x rays transmitted through the photocathode and the anode aperture and recorded directly on the streak-tube phosphor. The source of the signal immediately following the x-ray timing fiducial is unknown at this time.

Photocathode Response

In the limit that the ratio of the neutron absorption length to CH_2 layer thickness is large, the production rate of the recoil protons by neutron-elastic scattering will follow the neutron pulse shape. Therefore, the impulse response of the neutron streak-camera photocathode can be estimated by considering the elastic scattering as a simple binary collision and following the trajectories of the recoil protons, integrating over energy, direction, and initial position. The energy-angle dependence of the protons is given by the formula

$$E_p(\theta) = E_n \cos^2(\theta),$$

where E_p is the proton energy, E_n is the neutron energy, and θ is measured from the forward direction. The recoil protons (whose energies range from zero to the incident neutron energy) are not time resolved and recorded directly by the streak tube; instead, the recorded signal is produced by the low-energy secondary electrons generated by the energy loss of the protons in the thin CsI layer.

Proton-energy loss data as a function of proton energy can be obtained for most materials by interpolation in readily available tables of *dE/dx* values.[11] Given the proton energy-loss curves for the relevant materials, it is straightforward to numerically integrate the proton equation of motion and calculate the time, energy, position, and velocity of the recoil protons as they exit a slab of material. We assume simple nonrelativistic ballistics for the proton and do not include any secondary processes that may introduce straggling, a broadening in the angular and energy distributions. Neither subsequent interactions of the scattered neutrons nor proton-induced x-ray emission is included.

The neutron-sensitive photocathode response is determined from a histogram (by number and/or energy deposited) of the time and spatial position of the energy loss of the recoil protons in a 1000-Å-CsI layer. The initial proton-energy spectrum is flat. The protons are produced uniformly throughout a 1.0-mm-wide slab of CH_2 whose thickness is less than or equal to the maximum proton range, 3.0 mm and 122 μm for 14.1-MeV and 2.45-MeV protons, respectively. Only those proton trajectories that intersect the 1.0-mm-wide photocathode slit are counted. The proton time-of-flight is corrected for the neutron time-of-flight from the initial position of the recoil proton to the CsI layer. The impulse response and the point-spread function (PSF) of the photocathode weighted by energy deposited are presented in Fig. 53.15, for a range of CH_2 thicknesses over a 12.7-μm-thick Be substrate. Since the distribution of energy deposited per proton is fairly narrow (for detecting either DD or DT neutrons), the response calculated by number of events detected is essentially identical to that presented in Fig. 53.15. This implies that the secondary-electron current is linearly proportional to the neutron production rate.

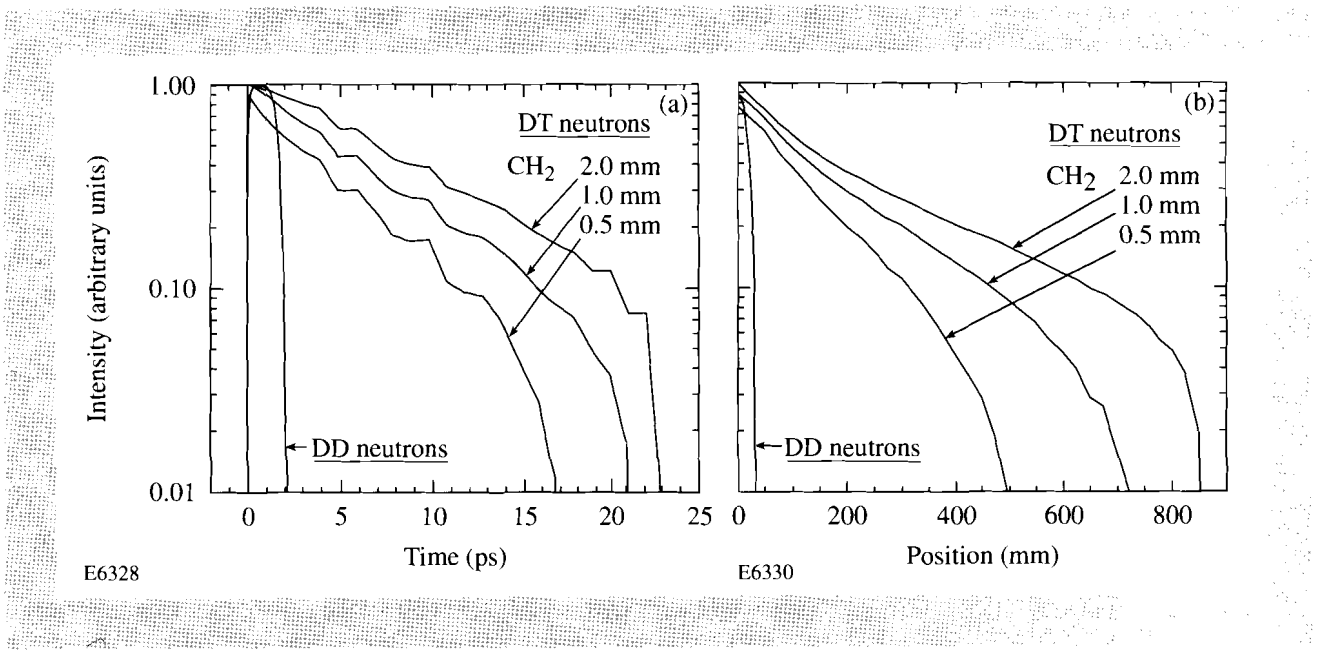

Fig. 53.15
(a) Temporal response of the neutron streak-camera photocathode to an impulse of 14.1-MeV and 2.45-MeV neutrons. The photocathode consists of a 1000-Å-CsI layer on a 12.7-μm-Be foil, which is backed with a 122-μm-CH_2 layer for the DD neutrons and 0.5 mm, 1.0 mm, and 2.0 mm of CH_2 for the DT neutrons. (b) Point-spread function for the same photocathode.

The temporal response to the DD neutrons is less than 2 ps and the maximum extent of the PSF is 30 μm. Nineteen percent of the protons produced in the 122-μm-thick CH_2 layer are detected in the CsI layer. The average energy of the protons entering the CsI layer is 1.0 MeV, and the average energy deposited per proton is 5.0 keV. The DT neutron response varies as expected with increasing CH_2 thickness; the sections nearest the Be/CsI layers contribute most efficiently. The overall detection efficiency of the protons produced in the CH_2 layer drops from 58% to 46% to 31% as the layer thickness increases from 0.5 mm to 1.0 mm to 2.0 mm. The temporal response increases marginally to 23 ps with CH_2 layer thickness, as does the maximum extent of the PSF to 850 μm. The average energy of the protons entering the CsI layer is 8.0 MeV, and the average energy deposited per proton is 1.75 keV. The response of the photo-

cathode to 14.1 MeV neutrons can be improved by replacing the 12.7-μm-Be substrate with a 100-μm-thick Au layer to moderate the protons. Temporal response is reduced to 10 ps and the extent of the PSF to 550 μm; however, the sensitivity also decreases by a factor of 2. We quote maximum values for the responses to hedge for the contribution of straggling effects, which are significant for large energy loss and/or low proton energy at the range limit.[12] These effects will be worse for detecting DT neutrons than for DD neutrons as the recoil-proton range is much larger. Simple estimates for the magnitude of the effect of straggling may be obtained by artificially modifying the energy loss in the CH_2 as the proton slows down. Low-energy stragglers are created by increasing the dE/dx values. This decreases the proton range and actually improves the photocathode response. High-energy stragglers have a longer range in the CH_2 and can double the temporal response and the PSF for a 2.0-mm-thick CH_2 layer; the responses with a 0.5-mm-thick CH_2 layer are degraded by about 50%. Replacing the Be substrate with a 100-μm-Au foil reduces the effects of straggling in the CH_2 layer to negligible magnitudes. For a DD neutron detector the degradation of the temporal response by energy straggling will not be worse than 8 ps—the stopping time for a 2.45-MeV proton in CH_2.

A simple estimate for the quantum efficiency of the CsI layer to the recoil protons can be made as follows. It has been shown experimentally that for protons (with energies ranging from 10 keV to tens of MeV) bombarding thin metal foils, the secondary-electron yield is proportional to the electronic stopping power within an accuracy of 10%.[13] dE/dx includes all the processes that contribute to the energy transferred to the electrons in the solid, which then cascades into secondary electrons. The forward-surface, secondary-electron yield for metals (Y_f) is approximately

$$Y_f = 0.017\, dE/dx,$$

where dE/dx is measured in keV/μm. The secondary-electron yield for proton bombardment of insulators is about ten times higher than for metals.[14] This can be understood because the secondary-electron mean-free paths are larger in insulators than in metals. Using the tabulated values of dE/dx to calculate the proton energy loss and a factor of 30 for the ratio of the secondary-electron yields for CsI to Au (as measured for x rays in the few-keV region[15]), we estimate that the number of secondary electrons emitted per event is 5–10 for DT neutrons and 15–25 for DD neutrons. The overall detection efficiency for DT neutrons is about a factor of 8 higher than for DD neutrons, mainly because of the larger ratio of the recoil-proton range to neutron cross section.

Experimental Results

The direct-drive target implosions were carried out using the 24-UV-beam OMEGA laser system. Typical parameters for the series of high-yield target experiments were 850 J to 1350 J in a 600-ps-FWHM Gaussian pulse delivered to a 320-μm-diam, 1.1-μm wall-thickness target filled with a 10-atm equimolar mixture of DT gas. These experiments produced 14.1-MeV neutron yields in the range of 3×10^{10} to 1×10^{11}. A few DD gas-filled targets were also imploded but the highest DD neutron yield for this series was 10^9 and no signal was observed.

Experimental results including the details of the neutron streak-camera photocathode are presented in Fig. 53.14. The streak record shows the bang-time x-ray emission followed 4.9 ns later by the DT neutron-generated recoil-proton signal. The neutron signal is clearly observable above the background level, which consists of some very bright speckles superimposed on a fairly uniform pedestal, outlined by the edge of the 40-mm-diam microchannel-plate (MCP) image intensifier. The neutron signal through the Be substrate is marginally brighter than through the Ta substrate; calculations predict a difference of 16%. Similarly, the section with 2.0 mm of CH_2 is predicted to be 37% brighter than the section with the 1.0-mm thickness. The streak speed for these preliminary experiments was 430 ps/mm at the output screen, to allow recording of a signal from the slower DD neutrons (13 ns after the x-ray signal). Although the slow streak speed severely limits the time resolution for the streak camera, there is a weak indication that the neutron signal recorded through the Ta substrate is slightly shorter than through the Be foil. A lineout through the reduced data is presented in Fig. 53.16. The high-energy, x-ray signal (filtered for E > 6 keV) is narrower than the 175-ps-FWHM neutron signal. The source of the emission peak 1 ns after the x-ray signal is unknown at this time. It is also present for non-neutron target shots and could perhaps be caused by x-ray fluorescence from plasma blow-off hitting the nose cone of the instrument.

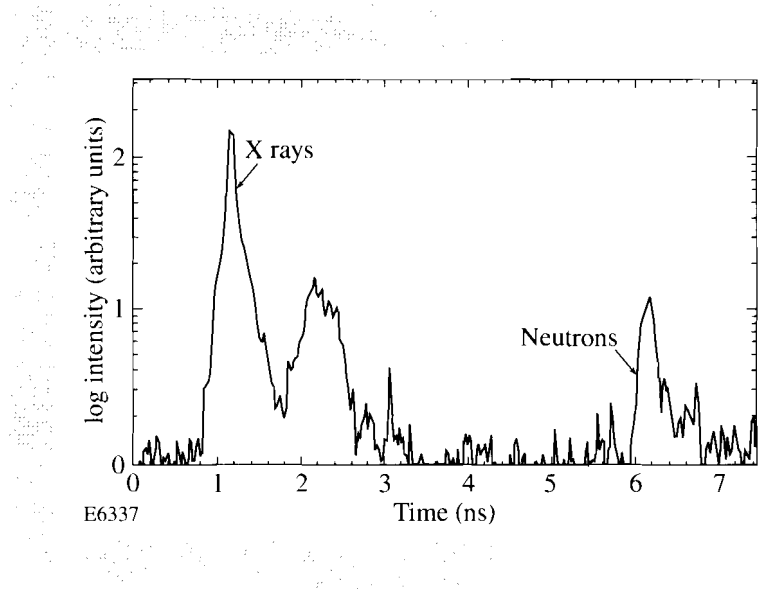

Fig. 53.16
Lineout of the x-ray bang-time signal followed 4.9 ns later by the neutron-generated signal. The source of the peak at $t = 2.5$ ns is unknown at this time.

The speckle noise in the recorded streak data is indicative of channel saturation in the MCP. Whether this is because of neutrons or γ rays interacting with the MCP itself, or with the streak-tube phosphor screen, and when it occurs (ns or μs after the implosion) needs to be investigated further. Similarly, the cause of the broad pedestal on the streak records needs to be resolved. Since the speckle is always positive valued, it can be easily removed. We use an algorithm that takes line segments in the spatial direction, calculates the average and standard deviation σ, and then replaces pixel values that exceed the average by more than 3σ with the average. This technique just clips the peaks and doesn't affect the time resolution of the streak record. Typically, two or three passes across the data

set are sufficient. Median or Fourier transform-filtering techniques would smooth out both the valleys and the peaks and thereby compromise the time histories. The broad pedestal is subtracted from the data after removing the speckle. As the streak camera is moved closer to target, the speckle noise will increase in the same ratio as the neutron signal and remain bothersome. Eventually the speckle and the pedestal will become problematic as they use up the available dynamic range of the recording system. To overcome this we are currently working on a new, small-diameter, large-aspect-ratio, streak-tube design that will allow us to get within 5 cm of a direct-drive target, and allow shielding to be placed between the neutron source and the phosphor/intensifier recording system.

Framing-Camera Neutron Detector

The concept of using a recoil-proton radiator as part of the photocathode in a neutron detector can also be applied to high-speed framing cameras (Fig. 53.17). These cameras use <100-ps duration, kilovolt electric pulses propagating along gold microstrip lines coated onto microchannel plates to generate 37-ps-duration frame times as described in articles 1.A and 1.B of this volume.[16] The CH_2 layer for such a detector would be in contact with the channel plate to minimize any time dispersion introduced by proton time-of-flight across a gap. The recoil proton would generate secondaries in the gold layer, which extends a channel diameter or so down the channel, or in the top surface layers of the channel itself. These secondary electrons are either quickly reabsorbed on the channel walls or, if the electrical pulse is present, accelerated down the channel and amplified. Sensitivity could be enhanced by a coating of CsI on the microstrip line. We don't anticipate any significant degradation of the voltage pulse on the strip line by having the proton radiator in contact.

Although the time resolution of the detector is limited to the frame time, the advantage of using this type of detector is the increased sensitivity available with a larger area sensor. The propagation speed of the electrical pulse down the strip line is 7 mm/35 ps. If the plate is tilted such that the electrical pulse propagation

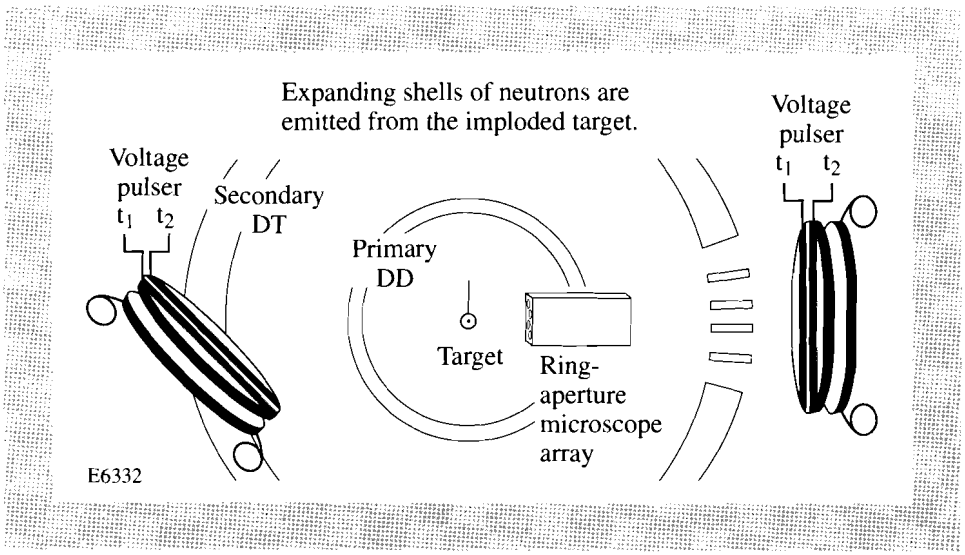

Fig. 53.17
Concept for a neutron-sensitive framing camera as a detector to measure both the primary and secondary burnwidths, or, when coupled to an array of neutron microscopes, to do time-resolved neutron imaging of the core.

direction is at 45° to the neutron velocity vector, the effective area per resolution element is 7 mm * sin 45° * width (7 mm) or 35 mm^2 (see Fig. 53.17). The plate is tilted to simplify synchronization of the gating pulse to the neutron signal; the time window is the length of the projection of the strip onto the neutron velocity vector divided by the neutron speed. At 45°, a 40-mm-long plate has a synchronization window for DT neutrons of 550±200 ps, depending on whether the electrical pulse propagation direction is toward or away from the target. The multiple strips available on the plates can be individually timed to allow overlapping frames or to detect primary- and secondary-neutron signals, which come at different times. With a pair of framing cameras separated by about 30 cm, one can conceive of performing ion-temperature measurements. The Doppler broadening of the DT neutron pulse is given by[17]

$$\Delta t(ps) = 1.2 * d(cm) * \sqrt{T_i(\text{keV})} ,$$

where d is the target-to-detector distance and T_i is the DT ion temperature. One just requires a resolvable broadening of the neutron pulse during the transit time between the pair of detectors. Another intriguing application of this technique is to take advantage of the narrow PSF for detecting DD neutrons and develop a high-speed, multiframe, neutron-imaging detector. The imaging could be accomplished with an array of penumbral-aperture,[18] or ring-aperture microscopes. Time-resolved neutron imaging should be possible for DD neutron yields >10^{12}.

The noise background with the framing-camera detector will potentially be less than for a streak-camera system because the gain element is on for a very short duration. In comparison, streak-camera intensifiers are generally active for 0.5 ms and integrate the long, low-level background signals.

Summary

We have demonstrated a prototype neutron streak camera capable of directly time-resolving the fusion-reaction burnwidth with an estimated time resolution <20 ps for DT neutrons and <10 ps for DD neutrons. The sensitivity of our recoil-proton radiator, close coupled to a CsI secondary-electron emitter, is comparable to detectors, based on coupling the emission from plastic scintillators to optical streak cameras, and orders of magnitude better than UO_2 photocathode-based detectors. The recoil-proton energy loss in the CsI layer follows the neutron production rate directly; there are no long-decay-time fluorescence emissions to deconvolve. Calculations indicate that the detector is about eight times more sensitive for recording DT neutrons than DD neutrons, making it favorable for recording primary- and secondary-neutron burnwidths on the same shot. We have also presented a concept for applying recoil-proton radiator photocathodes to high-speed framing cameras.

ACKNOWLEDGMENT

This work was supported by the U.S. Department of Energy Office of Inertial Confinement Fusion under Cooperative Agreement No. DE-FC03-92SF19460, the University of Rochester, and the New York State Energy Research and Development Authority. The support of DOE does not constitute an endorsement by DOE of the views expressed in this article.

REFERENCES

1. C. L. Wang, R. Kalibjian, and M. S. Singh, in *15th International Congress on High Speed Photography and Photonics* (SPIE, Bellingham, WA, 1982), Vol. 348, p. 276.
2. C. L. Wang *et al.*, Rev. Sci. Instrum. **56**, 1096 (1985).
3. C. L. Wang *et al.*, Rev. Sci. Instrum. **57**, 1749 (1986).
4. H. Niki *et al.*, Rev. Sci. Instrum. **57**, 1743 (1986).
5. K. Kinoshita *et al.*, in *High Speed Photography, Videography, and Photonics IV* (SPIE, Bellingham, WA, 1986), Vol. 693, p. 111.
6. N. Miyanaga *et al.*, Rev. Sci. Instrum. **61**, 3592 (1990).
7. J. N. Anno, J. Appl. Phys. **33**, 1678 (1962).
8. D. R. Kania, S. M. Lane, and S. G. Prussin, Appl. Phys. Lett. **53**, 1988 (1988).
9. H. Azechi *et al.*, Appl. Phys. Lett. **55**, 945 (1989).
10. R. A. Lerche, M. D. Cable, and D. W. Phillion, Rev. Sci. Instrum. **61**, 3187 (1990).
11. H. Bichsel, in *American Institute of Physics Handbook* (McGraw-Hill, New York, 1972), Chap. 8d, pp. 8-142–8-189.
12. D. D. Cohen and E. K. Rose, Nucl. Instrum. & Methods Phys. Res. **B64**, 672 (1992).
13. H. Rothard, K. O. Groeneveld, and J. Kemmler, in *Particle Induced Electron Emission II* (Springer-Verlag, Berlin, 1991), Vol. 123, p. 97.
14. D. Hasselkamp, in *Particle Induced Electron Emission II* (Springer-Verlag, Berlin, 1991), Vol. 123, p. 66.
15. B. L. Henke, J. P. Knauer, and K. Premaratne, J. Appl. Phys. **52**, 1509 (1981).
16. D. K. Bradley, P. M. Bell, J. D. Kilkenney, R. Hanks, O. Landen, P. A. Jaanimagi, P. W. McKenty, and C. P. Verdon, Rev. Sci Instrum. **63**, 4813 (1992).
17. H. Brysk, Plasma Phys. **15**, 611 (1973).
18. D. Ress *et al.*, Rev. Sci. Instrum. **61**, 3184 (1990).

1.D Nuclear Diagnostics for the OMEGA Upgrade

The OMEGA Upgrade 60-beam glass laser facility, currently under construction at the University of Rochester, will be capable of symmetrically illuminating a direct-drive ICF target with 30 kJ of highly spatially uniform, temporally pulse-shaped, 351-nm light.[1] The OMEGA system currently employs several

diagnostics to measure the flux and energy spectra of neutrons emitted from the target. These measurements have enabled us to infer fuel ion temperature, and fuel and shell areal density. Analysis of data from nuclear diagnostics has provided many insights into the performance of laser-fusion targets.

The Upgrade will include a full array of neutron diagnostics and will be constructed with special provisions to increase the usability and accuracy of the nuclear instrumentation.

In the previous article, the development of time-resolved neutron diagnostics was discussed. In this article we describe the time-integrated neutron diagnostics planned for two out of the 32 total diagnostic ports on the OMEGA Upgrade. One of these ports (the "line-of-sight" port) will have a plastic collimator mounted to it that will provide a low-scattered-neutron location for several short-path (2- to 4-m) time-of-flight detectors. These detectors will be used primarily to measure ion temperatures for high-yield ($>10^7$) DD fuel-target experiments. (Fig. 53.18). A path through this collimator is available for long-path (20-m), time-of-flight instruments that are to be housed in a separate building outside of the target-bay shield wall (Fig. 53.19). This wall serves as a 1-m-thick second collimator for this diagnostic building. The neutron-diagnostic building and target bay have provisions for the attachment of a flight tube to minimize the effects of neutron scattering along the latter part of the flight path. We are currently planning radiation-transport analysis to optimize the design of the collimators for this system. The instruments in the diagnostic room will be used to measure DT and DD ion temperature and DD secondary spectra.

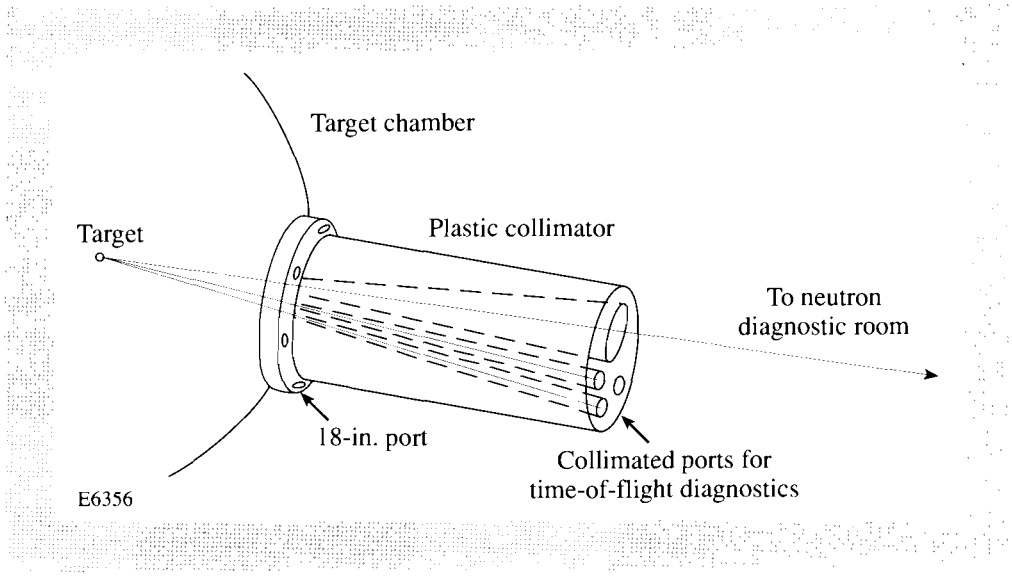

Fig. 53.18
A first collimator for time-of-flight neutron diagnostics will be mounted on the target chamber.

Neutron spectra will be measured to infer fuel-ion temperature and, through measurement of the secondary reaction products,[2] fuel areal density. The primary instruments used to measure neutron spectra are single scintillator/fast photomultiplier combinations ("current"-mode detectors), and arrays of scintillators and photomultipliers operated in "single-hit" mode. The current-

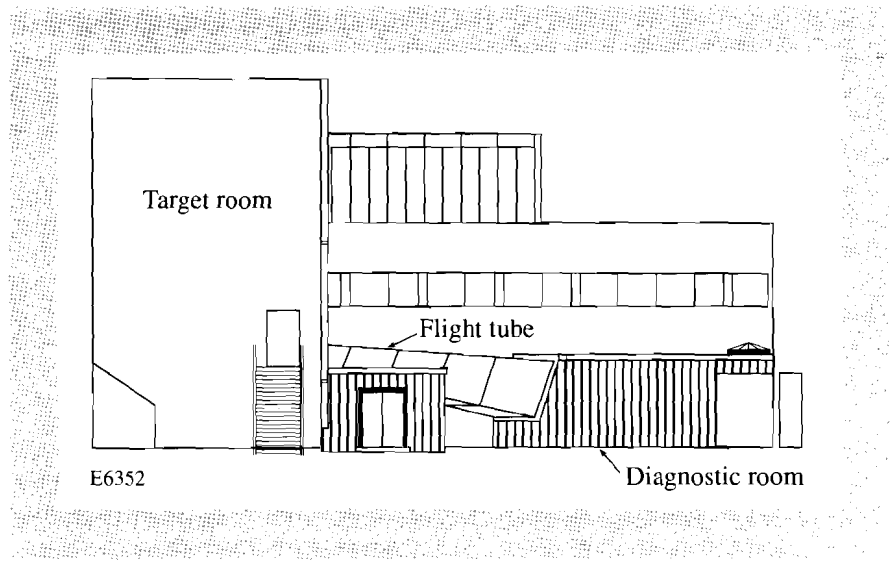

Fig. 53.19
A neutron diagnostic room is being constructed that will provide a time-of-flight path length of 20 m.

mode detectors (described in previous issues of the LLE Review[3]) have limited accuracy at low neutron yields because there are few detected events in the necessarily small scintillator volume. Increasing the size of the scintillator reduces the time resolution because of multiple light reflections within the scintillator crystal. For this reason, ion temperatures at low neutron yields and secondary neutron spectra will be measured using a multi-detector array technique developed at LLNL.[4] We have developed and tested a 96-channel prototype of the array planned for the Upgrade facility.[5] Typical ion-temperature data for this array are shown in Fig. 59.20. A single-hit array is currently being constructed that consists of 960 photomultiplier plastic-scintillator detectors. For each channel the time of arrival of the neutron event is recorded, creating an energy histogram. We also record the amplitude of the signal received in each channel, both to enable operation as a large current-mode detector and for amplitude-based timing corrections (Fig. 59.21). The neutron-diagnostic room was designed specifically to house this large detector array and two to three current-mode detectors and their associated electronics.

The other diagnostic port allocated for neutron instrumentation will contain activation diagnostics and a rapid extraction mechanism for target debris collection (Fig. 59.22). Neutron yield from the primary branch of the nuclear reaction for DD or DT fuel will be measured by indium and copper activation, respectively. Because the gamma spectrometers (counters) for these activation detectors are located in a low-background shielded area beneath the target chamber and because of the possibility of dangerous levels of radioactivity in the target chamber after a high-neutron-yield target experiment, automatic drop systems will be constructed to transport the activated samples from the target chamber to the counters (see Fig. 59.23). Measurement of activated target debris collected during a target implosion has been used to measure shell areal density[6] and fuel areal density.[7] A rapid extractor will be constructed to remove collected target debris from the vacuum of the target chamber to the counting area beneath the target chamber. The transport system will be capable of moving the sample to the counting area in under 30 s, to enable counting of short half-life isotopes.

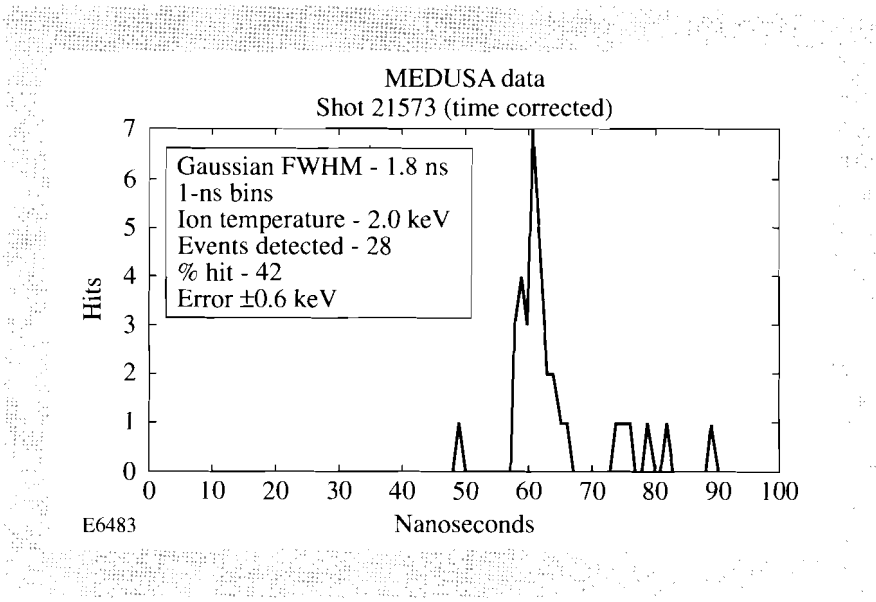

Fig. 53.20
Ion temperature data from the prototype (96-channel), single-hit detector agrees with current-mode detector.

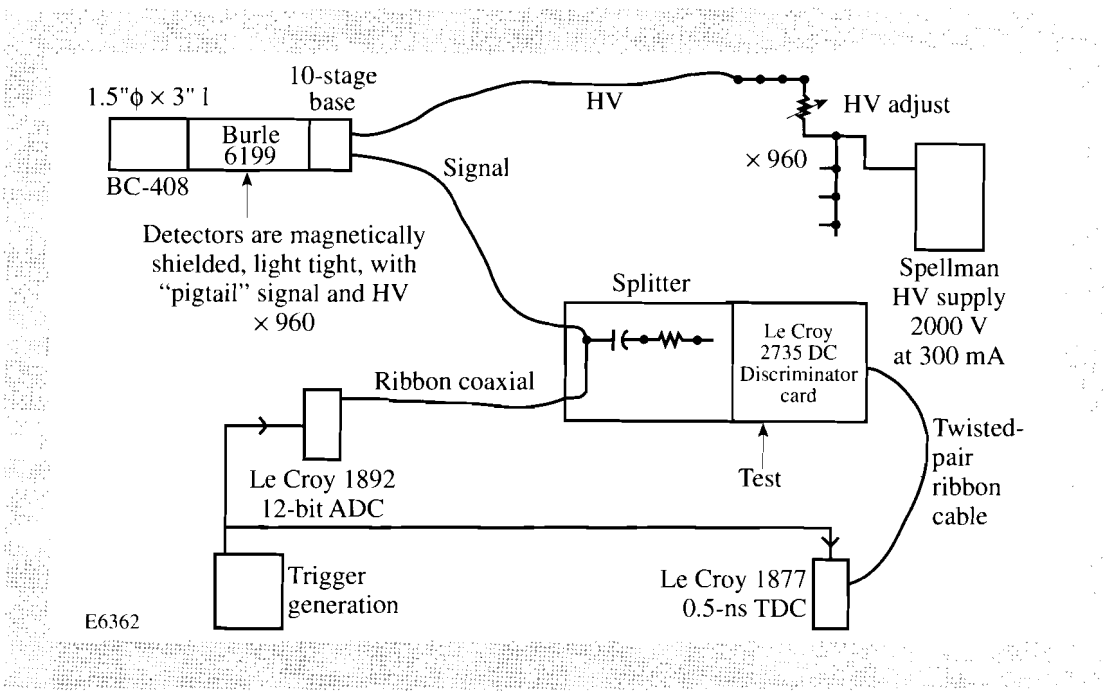

Fig. 53.21
Analog-to-digital converters and time-to-digital converters provide amplitude and time data for each of the 960 channels of Upgrade MEDUSA.

We have three detectors for gamma spectroscopy: a large (25 cm × 25 cm) sodium iodide detector for high-sensitivity, low-resolution requirements, and two high-purity germanium detectors for high-resolution spectroscopy.

A measurement of the response function of the previously mentioned detectors to single neutrons is essential for unambiguous unfolding of the measured data.

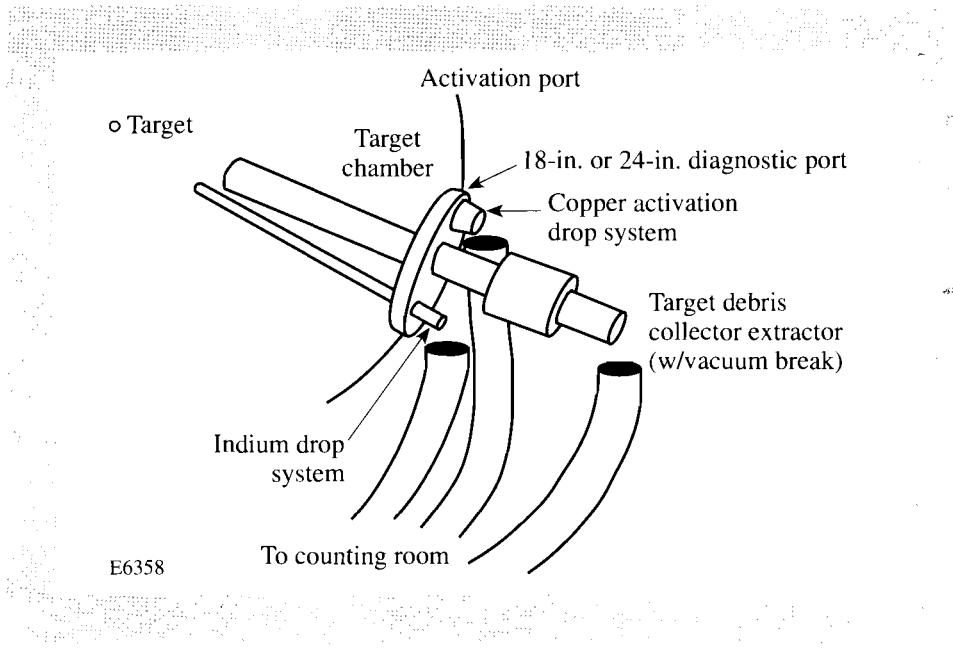

Fig. 53.22
A chamber will contain activation diagnostics and a radiation-chemistry collector extractor.

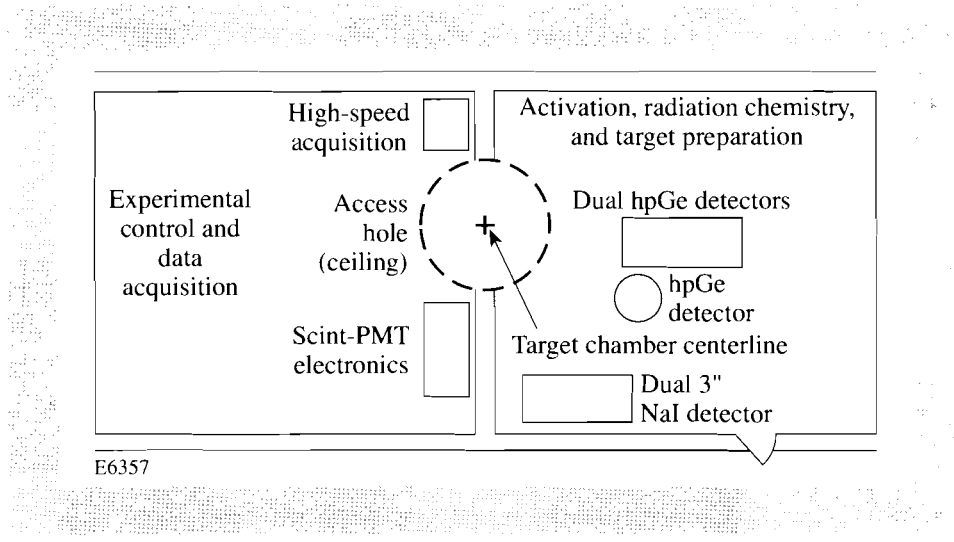

Fig. 53.23
Activated material will be analyzed in a low-background counting room beneath the target chamber.

A calibration facility capable of producing 2.45-MeV (DD) and 14.1-MeV (DT) neutrons is essential. We have begun a collaboration with SUNY Geneseo to construct a calibration facility capable of producing sub-5-ns bursts of neutrons from the Geneseo 2-MV VanDeGraff accelerator. Short bursts of neutrons are highly desirable since the effects of neutron scattering in the accelerator, experiment room, and surrounding materials may then be eliminated by time gating of the signal from the detector under calibration. This VanDeGraff is capable of stable operation at accelerating voltages as low as 100 kV, which is important to the optimization of neutron yield in each calibration pulse, since the

neutron-production cross sections peak in this energy range. A buncher/chopper beamline has been designed by National Electrostatics Corporation that will produce sub-5-ns pulses at a 4-MHz repetition rate. The target room for the VanDeGraff was designed for neutron production experiments and has the necessary size and shielding for unambiguous calibration of all our planned detectors. The 25-mile distance to the Geneseo campus and ready availability of operating time on the accelerator is a great advantage in rapid turnaround of calibration data.

In summary, we have taken steps to ensure that the neutron diagnostics for the OMEGA Upgrade will meet the needs of the laser-fusion program at LLE. Dedicated target-chamber ports and a neutron flight path will allow control over the scattered-neutron environment in the remote diagnostic room. Diagnostics that require the higher neutron yields expected from the Upgrade, such as the single-hit detector array to measure secondary neutron energy spectra, are now being designed. Diagnostics currently on OMEGA are being redesigned for the Upgrade target chamber and for remote operation in the case of dangerous levels of radioactivity in the target bay. Finally, the availability of a reliable calibration facility at SUNY Geneseo is a great asset in the careful characterization of all the neutron detectors.

ACKNOWLEDGMENT

This work was supported by the U.S. Department of Energy Office of Inertial Confinement Fusion under Cooperative Agreement No. DE-FC03-92SF19460 and the University of Rochester. The support of DOE does not constitute an endorsement by DOE of the views expressed in this article.

REFERENCES

1. LLE Review **39**, 114 (1989).
2. T. E. Blue and D. B. Harris, Nucl. Sci. Eng. **77**, 463 (1981).
3. LLE Review **27**, 103 (1986); LLE Review **36**, 150 (1988).
4. M. D. Cable and S. P. Hatchett, J. Appl. Phys. **62**, 2233 (1987).
5. R. L. Kremens and M. A. Russotto, presented at the 33rd Annual Meeting of the American Physical Society, Plasma Physics Division, Tampa, Fl, 4–8 November 1991.
6. S. M. Lane, E. M. Campbell, and C. Bennett, J. Appl. Phys. **56**, 2027 (1984).
7. H. Azechi *et al.*, Appl. Phys. Lett. **49**, 555 (1986).

1.E Temporal Pulse-Width Control of the OMEGA and GDL Laser Oscillators

Flexibility in shaping the temporal profile of the optical pulses applied to laser-fusion targets is a goal for the OMEGA Upgrade. There are several schemes proposed to provide this flexibility.[1–3] The scheme implemented on OMEGA and currently being implemented on GDL involves producing an optical pulse with a laser oscillator and then modifying the temporal profile of this pulse outside the laser oscillator. The final temporal profile depends critically on the

input temporal profile to the pulse-shaping apparatus; that is, it depends on the temporal profile of the pulse out of the laser oscillator. The temporal profile of a pulsed laser depends on the detailed parameters of the laser cavity and intracavity components. Pulse-width control of the current laser oscillators is accomplished through the use of intracavity Fabry-Perot etalons.[2]

On the current OMEGA laser system a short pulse of approximately 70-ps FWHM is produced in a continuous-wave (cw), mode-locked laser and injected into a regenerative amplifier (regen). In the regen the pulse width is stretched with an intracavity Fabry-Perot etalon and amplified to the millijoule level. The output of the regen is then given a steep rising edge by triggering a fast Pockels cell, which removes energy from the beginning of the pulse.[3] In GDL, two regens will be used to produce the main and foot pulses. The two regens will be seeded from the same cw mode-locked laser to maintain synchronization of their output pulses. The two regens differ mainly in the width of their output pulses. The individual pulse widths of the main- and foot-pulse regens will again be controlled by intracavity Fabry-Perot etalons. Until now, little success has been had in analyzing the temporal-mode structure of a laser incorporating one or several etalons.

The Fabry-Perot Etalon

An interferometer consisting of two plane-parallel reflecting surfaces constitutes a Fabry-Perot etalon. The steady-state operation of a Fabry-Perot etalon is well known.[4] For cw input the series of partial waves emitted from an etalon can be summed in closed form to obtain the Airy formula. Concepts such as the free spectral range and the finesse of the etalon are then well defined and can be derived from the Airy formula. When using short pulses or pulses with temporal or phase modulation, a transient analysis is necessary. A rigorous treatment of the transient response of an etalon requires the use of linear systems theory.[5]

When a wave is incident on a plane-parallel etalon, a series of partial waves are transmitted as well as reflected from the etalon. When an etalon is inserted into a laser cavity, it is adjusted so that its surface makes a small angle with the beam lasing in the cavity. If one of the laser end mirrors is flat, tilting the etalon will not misalign the laser cavity in principle since the transmitted waves from the etalon exit the etalon parallel to the input wave regardless of the magnitude of the tilt angle (albeit with some slight translation). On the other hand, the reflected partial waves from the etalon are reflected at a small angle (twice the tilt angle) to the incident wave. The reflected waves from the etalon will eventually be blocked by a limiting aperture in the laser cavity and will be prevented from lasing. For this reason, in the following analysis we only need to consider the transmitted waves through the etalon. The analysis, however, can easily be modified to include a resonant reflector where the reflected waves from the etalon contribute to the laser oscillation.

By the superposition principle for electric fields, the partial waves that exit from an etalon must be added coherently to determine the total output field. This is a linear process, and hence, an etalon comprises a linear system that can be

analyzed using the formalism of linear systems theory.[5] To determine the output of a linear system we need to calculate the impulse-response function of the system. The impulse-response function of an etalon can be determined by calculating the output of the etalon for a delta function input $\delta(t)$ at time equals zero. The impulse-response function of an etalon having thickness d, surface-amplitude transmissions γ_1 and γ_2, and surface-amplitude reflectivities r_1 and r_2 is given by[6]

$$h(t) = \Gamma \sum_{m=0}^{\infty} R^m \exp(i2mkc\tau)\, \delta(t - 2m\tau)\,, \tag{1}$$

where $\tau = dn\cos\theta/c$ is the transit time through the etalon, c is the speed of light in vacuum, n is the refractive index of the etalon substrate, k is the wave number (if the radiation has some finite spread in time then k is interpreted as the wave number at the central wavelength of the associated bandwidth), θ is the angle between the normal to the etalon surface and the incident beam, and $R = r_1 r_2$ and $\Gamma = \gamma_1\gamma_2$ with $\Gamma = 1 - R$. The output of the system is given by the convolution

$$E_{\text{out}}(t) = h(t) * E_{\text{in}}(t) = \int_{-\infty}^{\infty} h(\alpha) E_{\text{in}}(t - \alpha)\, d\alpha \tag{2}$$

of the input field $E_{\text{in}}(t)$ with the impulse-response function. Performing this operation gives

$$E_{\text{out}}(t) = \Gamma \sum_{m=0}^{\infty} R^m \exp(i2mkc\tau)\, E_{\text{in}}(t - 2m\tau) \tag{3}$$

for the temporal profile of the output optical field. This equation represents the operation of an etalon on an input optical field to produce an output optical field.

For the special case when E_{in} is constant, that is for cw input, the summation in Eq. (3) can be performed in closed form and the result leads to the Airy formula. The physical interpretation of Eq. (3) is straightforward in terms of the coherent summation of partial waves and is given in the literature.[4]

For the more general case when the input to the etalon is an optical pulse, that is $E_{\text{in}}(t)$ has some temporal profile, the output temporal profile from the etalon again consists of an infinite coherent summation of partial waves. As seen in Eq. (3), each partial wave consists of the input field, translated in time by the etalon round-trip transit time, with amplitude progressively reduced by the reflectivity of the etalon surfaces. For a pulse whose width is of the order of the etalon transit time, severe pulse distortion will occur in the output from the etalon. Figure 53.24 shows the calculated output-intensity temporal profile from an etalon with an input Gaussian-intensity temporal profile having a FWHM pulse width equal to the etalon single-pass transit time. The etalon in this case has surface-intensity reflectivities of 80%, and it is assumed that all partial waves add in phase so that the phase term in Eqs. (1) and (3) is unity. In general, the output

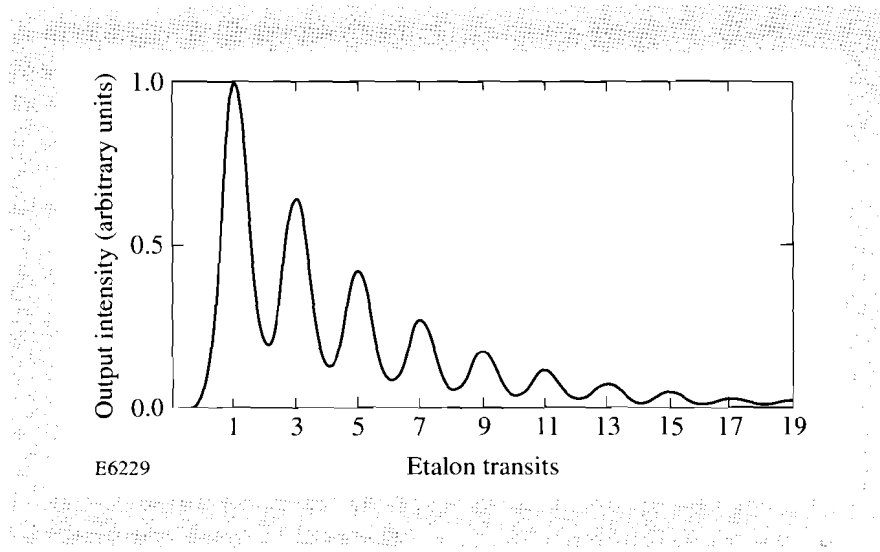

Fig. 53.24
The output-intensity profile from an etalon with an input Gaussian-intensity profile having a FWHM pulse width equal to the etalon single-pass transit time.

of an etalon is stretched in time with a right-left asymmetry in the pulse shape and with some degree of temporal modulation, as illustrated in Fig. 53.24. The temporal modulation and the right-left asymmetry have been observed in the output of a regenerative amplifier and are discussed in the experimental section.

In a regenerative amplifier with an intracavity etalon, a short pulse (short compared to the laser-cavity round-trip time) is injected into the laser cavity and makes many round trips in the cavity. This pulse is amplified and operated on by the etalon during each pass in the laser cavity. The temporal profile of the pulse in the cavity can be calculated after each pass from Eq. (3) given the input temporal profile to the etalon. The output profile from the etalon after each pass becomes the input profile to the etalon for the next pass. Knowing the injected pulse temporal profile, the process can be iterated for each laser-cavity round trip to determine the final output temporal profile of the regenerative amplifier. If the final pulse width emitted by the regenerative amplifier is comparable to the regenerative-amplifier cavity round-trip transit time, then the effects of the regenerative-amplifier cavity on the pulse width must be taken into account.

Etalons Inside a Laser Cavity

An intracavity etalon can be used to increase the pulse width emitted by a regenerative amplifier. If the temporal pulse width of the radiation in the regenerative-amplifier laser cavity becomes of the order of the laser-cavity round-trip time, then the effect of the laser cavity itself must be taken into consideration. This can be accomplished by calculating the impulse-response function for a single pass or for a round trip through the laser cavity including the etalons, and then iterating this for each pass or laser-cavity round trip as previously described.

To calculate the impulse-response function for a round trip in the laser cavity we begin by tracing a delta-function input around the laser cavity in a round trip. We decompose the laser-cavity round-trip operation into space propagation and the operation of the etalons. The laser-cavity round-trip propagation is shown

schematically in Fig. 53.25 as five separate operations. The operations with their impulse-response functions are $h_{L1}(t)$ for propagation from the end mirror to the etalon and through the etalon for propagation over an optical distance $L1$, $h_e(t)$ for the operation of the etalon, $h_{L2}(t)$ for propagation from the etalon to the end mirror and back to the etalon and through the etalon for propagation over an optical distance $L2$, $h_e(t)$ for the second operation of the etalon, and $h_{L3}(t)$ for propagation back to the first mirror over a distance $L3$. If we cascade the previously mentioned operations (the convolutions can be performed in any order) we obtain the impulse-response function corresponding to a round trip in the laser cavity given by

$$h_s(t) = h_{L1}(t) * h_{L2}(t) * h_{L3}(t) * h_e(t) * h_e(t). \tag{4}$$

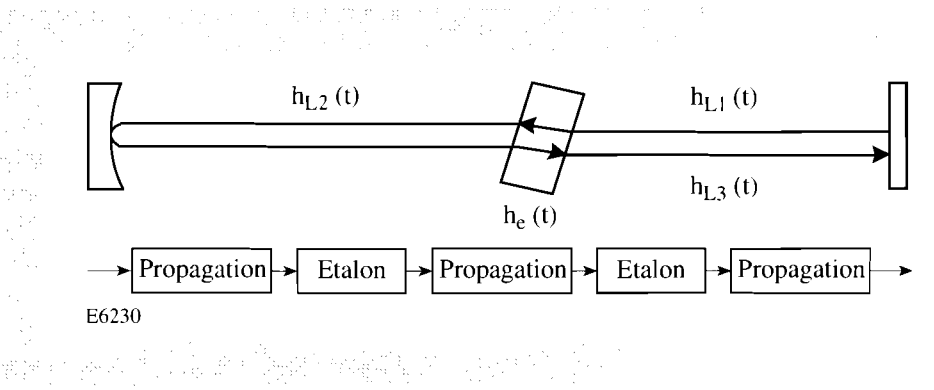

Fig. 53.25
The impulse-response function corresponding to a round trip in a laser cavity with an intracavity etalon represented as a cascade of five operations in the laser cavity.

The impulse-response function corresponding to propagation over the optical distance L is given by

$$h_L(t) = \alpha\, \delta(t - \tau_L) \exp(ikL), \tag{5}$$

where τ_L is the propagation time over the optical distance L, and α represents the linear amplitude gain or loss in the propagation. Equation (4) with Eq. (5) for the individual space propagations and Eq. (1) for the operation of the etalon gives

$$h_s(t) = \Gamma_c \Gamma^2 \exp(ikL) \sum_{\ell=0}^{\infty} \sum_{m=0}^{\infty} R^{(m+\ell)} \exp\left[i2kc\tau(m+\ell)\right] \delta\left[t - \tau_c - 2\tau(m+\ell)\right] \tag{6}$$

for the system impulse-response function, where $\Gamma_c = r_{1c} r_{2c} \gamma_{1c}$ is the product of the laser-cavity end-mirror amplitude reflectivities r_{1c} r_{2c} and amplitude transmission γ_{1c} of the laser-output coupler, $L = L1 + L2 + L3$ is the total round-trip optical distance in the laser cavity (including etalons), $\tau_c = \tau_1 + \tau_2 + \tau_3$ is the laser-cavity round-trip time, and the remainder of the variables are defined as in Eq. (3). The output of the system after one laser-cavity round trip is then given by

$$E_{\text{out}}(t) = \Gamma_c \Gamma^2 \exp(ikL) \sum_{\ell=0}^{\infty} \sum_{m=0}^{\infty} R^{(m+\ell)} \exp\left[i2kc\tau(m+\ell)\right] E_{\text{in}}\left[t - \tau_c - 2\tau(m+\ell)\right] \tag{7}$$

in terms of the input to the system and the appropriate variables as defined previously. Often times it is necessary to insert two etalons in the laser cavity. With a straightforward extension of the preceeding procedure we obtain the expression

$$E_{\text{out}}(t) = \Gamma_c \Gamma_{e1}^2 \Gamma_{e2}^2 \exp(ikL) \sum_{\ell_2=0}^{\infty} \sum_{m_2=0}^{\infty} \sum_{\ell_1=0}^{\infty} \sum_{m_1=0}^{\infty} R_{e1}^{m_1+\ell_1}$$

$$R_{e2}^{m_2+\ell_2} \exp\left[i2kc\tau_{e1}(m_1+\ell_1)\right]$$

$$\exp\left[i2kc\tau_{e2}(m_2+\ell_2)\right] E_{\text{in}}\left[t-\tau_c-2\tau_{e1}(m_1+\ell_1)-2\tau_{e2}(m_2+\ell_2)\right] \quad (8)$$

for the output of a regenerative amplifier with two etalons. [Equation (8) assumes a "cold cavity" with no gain. When operating in the small-signal gain region of the laser and for an injected pulse having a narrow bandwidth compared to the gain bandwidth, the gain will only affect the amplitude of the output pulse and not the temporal profile. This is a good approximation for the experiments described in the experimental section.] In Eq. (8) there are two summations for each etalon since the etalons are double passed in one laser-cavity round trip. Further generalizations to a laser cavity with several etalons are straightforward. Note that the no-etalon case corresponds to the ℓ_1, m_1, ℓ_2, and $m_2 = 0$ term in Eq. (8). This term reduces to Eq. (5) and corresponds to propagation over the round-trip distance L in the laser cavity, where L becomes twice the laser-cavity length and τ_c becomes the laser-cavity round-trip time with kL the accumulated phase on a round trip. For the case when the final pulse width is of the order of the laser-cavity round-trip time or larger, the oscillator condition requires that the phase shift on a round trip through the laser cavity be an integer multiple of 2π (i.e., $kL = p2\pi$ for p an integer). For optimum injection in this case, we require that the laser-cavity length be an integer multiple of the center wavelength of the injected pulse into the regenerative amplifier and that the etalon be tuned for maximum transmission at this wavelength.

Thermal Sensitivity

To determine the temperature sensitivity of a regenerative amplifier with an intracavity etalon we examine the thermal-mechanical properties of the etalon. When a regenerative amplifier is aligned, the etalon is angle tuned such that the partial waves from the etalon all add in phase. If the temperature drifts after the initial alignment, the operation of the etalon changes and an effective loss will be introduced into the regenerative-amplifier laser cavity. Both the index of refraction n and the etalon thickness d_e depend on temperature. The exact treatment of the temperature sensitivity of a regenerative amplifier with an intracavity etalon is complex. To approximate the temperature sensitivity of an etalon we examine the change in the output field [given by Eq. (3)] for a small change in temperature. If we allow the output field represented by Eq. (3) to depend on temperature and expand the optical path length in the etalon about ΔT (keeping only the lowest-order terms), then the field at a slightly different temperature $T + \Delta T$ can be approximated by

$$E_{\text{out}}(t,\ T+\Delta T) = \Gamma \sum_{m=0}^{\infty} R^m \exp\left\{ i2mk\left[nd_e + \frac{d(nd_e)}{dT}\,\Delta T \right] \right\} E_{\text{in}}(t - 2m\tau) \quad . (9)$$

Here we have only considered the change in the phase relationship of the partial waves exiting the etalon and have neglected the change in transit time τ in the last factor of Eq. (3). This small change in temperature causes the small change $\left[d(nd_e)/dT\right]\Delta T$ in the single-pass optical path length through the etalon. If the single-pass optical path length through the etalon changes by one-half wavelength, then the etalon will tune through one free spectral range. The temperature change required to change the bandpass of the etalon by one free spectral range is then given by

$$\Delta T = \frac{\lambda/2}{\left[\dfrac{d(nd_e)}{dT}\right]} = \frac{\lambda/2}{\left[n\,\dfrac{d(d_e)}{dT} + d_e\,\dfrac{d(n)}{dT}\right]} \qquad (10)$$

For a 4-mm fused-silica etalon $n = 1.45$, $1/d_e\ d(d_e)/dT = 0.55 \times 10^{-6}/°C$, $dn/dT = 10.3 \times 10^{-6}/°C$,[7] and for $\lambda = 1053$ nm we get $\Delta T = 11.9°C$ to tune the etalon through one free spectral range. This value has been verified experimentally and is discussed in the next section.

Experiment

Verification of the preceeding theory has been performed through a series of experiments with intracavity etalons. A set of fused-silica etalons having 50% reflecting surfaces and varying thicknesses were tested in a regenerative amplifier. The surfaces of the etalons were coated in two coating runs (one per surface) to ensure uniformity of the reflective coatings among the etalons. The etalons were temperature controlled to within 0.1°C in order to stabilize their properties. An Nd:YLF regenerative amplifier was seeded with a 70-ps-FWHM pulse from a cw mode-locked Nd:YLF laser. Pulses from the cw mode-locked laser were injected into the regenerative amplifier by polarization coupling off the regenerative-amplifier intracavity polarizer. At the peak of the gain profile of the flash-lamp-pumped Nd:YLF rod, a pulse was locked into the laser cavity by rapidly changing the state of the laser-cavity Q-switch in less than the laser-cavity round-trip time. Once locked in the laser cavity, the injected pulse experienced gain and was operated on by the intracavity etalons during each successive round trip in the laser cavity. The 50% reflecting end mirror of the regenerative amplifier was used as an output coupler. The injected pulse made several round trips in the laser cavity, after which a Q-switched, mode-locked-type pulse train was emitted with pulses in the pulse train separated by the laser-cavity round-trip time of 13 ns. The buildup time of the laser cavity (i.e., the time between when the pulse is locked into the laser cavity until the pulse is emitted by the laser cavity) was measured to determine the number of round trips that the injected pulse made in the laser cavity.

The buildup time of the regenerative amplifier could be changed by varying the gain in the laser rod. Decreasing the gain causes the buildup time to increase, and conversely, increasing the gain causes the buildup time to decrease. Figure

53.26 shows the FWHM output pulse width of the regenerative amplifier versus the number of round trips that the injected pulse makes in the laser cavity for a 4-mm etalon. Also shown in this figure is the left-half width at half maximum (left HWHM) and right-half width at half maximum (right HWHM) for each data point. The left HWHM is the half width of the beginning of the pulse and the right HWHM is the half width of the end of the pulse. The solid curves in the figure correspond to the previously mentioned theory with the upper curve corresponding to the FWHM of the pulse, the center curve corresponding to the right HWHM of the pulse, and the lower curve corresponding to the left HWHM of the pulse. Note that after just one round trip in the laser cavity the pulse develops a left-right asymmetry in the pulse temporal profile indicating a sharper rising edge than falling edge. This is as expected from the discussion on the operation of a single etalon. This asymmetry persists but does not change significantly as the number of round trips in the laser cavity increases.

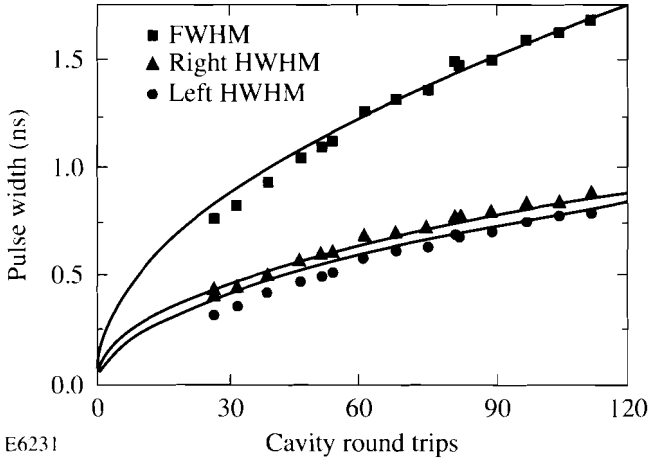

Fig. 53.26
The output pulse width of a regenerative amplifier with 4-mm intracavity etalon plotted versus the number of round trips the injected pulse makes in the laser cavity. The solid curves correspond to a calculation of the pulse FWHM (upper curve), right HWHM (middle curve), and left HWHM (lower curve). The left- and right-half widths show the asymmetry in the pulse profile.

Figure 53.27 shows the output pulse width of the regenerative amplifier versus the etalon thickness for the set of etalons. All measurements in Fig. 53.27 were taken with the same buildup time corresponding to 27 laser-cavity round trips for the injected pulse. The solid curve in the figure corresponds to the previously mentioned theory with the appropriate experimental conditions.

For a single, thick intracavity etalon (i.e., the injected pulse width is shorter than the etalon transit time) severe temporal modulation is observed. Figure 53.28 shows the output of the regenerative amplifier for the 25.4-mm etalon taken with a 4.5-GHz SCD5000 Tektronix digitizing oscilloscope and a fast vacuum photodiode (response time approximately 100 ps). The injected pulse made approximately 60 round trips in the laser cavity. For this case, the 70-ps, FWHM-injected pulse is shorter than the 123-ps etalon transit time. As seen in Fig. 53.28, the output of the regenerative amplifier has the temporal modulation expected from an iteration of Eq. (3) and as depicted in Fig. 53.24 for a similar case. Figure 53.29 shows a calculation of the pulse temporal profile for this case

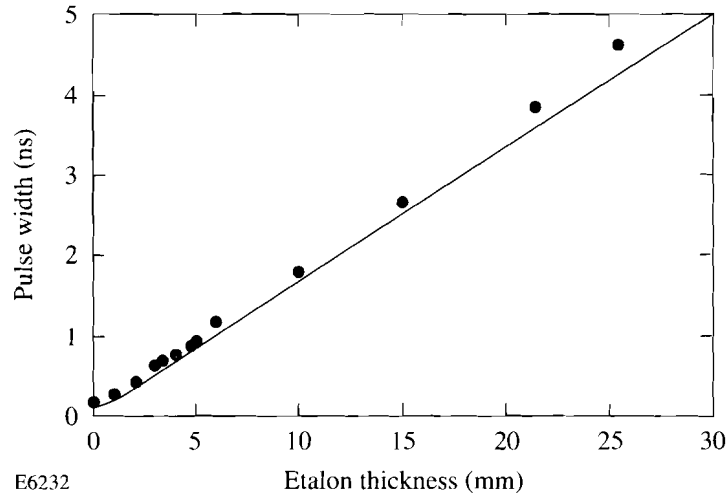

Fig. 53.27
The output pulse width (FWHM) of a regenerative amplifier with intracavity etalon plotted versus the etalon thickness. The injected 70-ps pulse (FWHM) made 27 round trips in the regenerative-amplifier cavity. All etalons were fused silica with 50% reflective coatings on both surfaces.

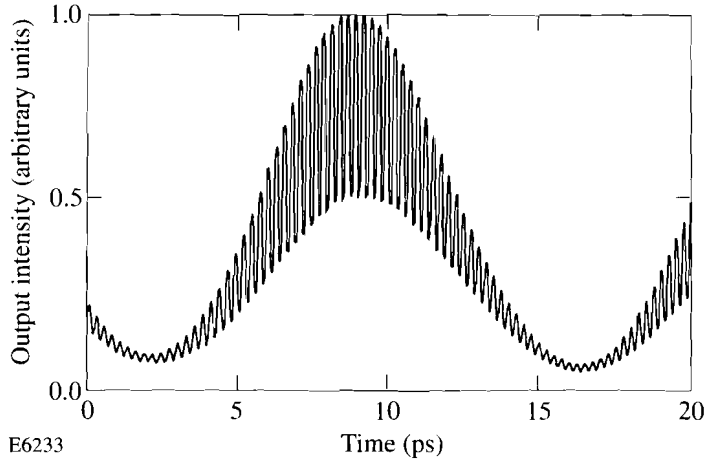

Fig. 53.28
The measured output-intensity temporal profile of a regenerative amplifier with a 25.4-mm intracavity etalon. The response time of the detection system was approximately 100 ps.

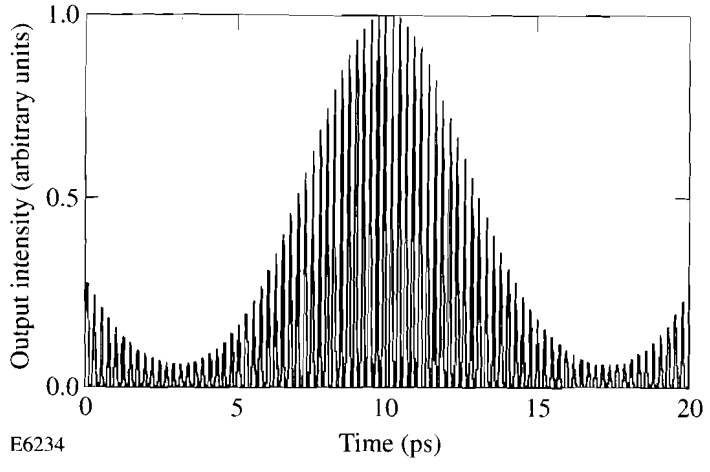

Fig. 53.29
The calculated output-intensity temporal profile of a regenerative amplifier with a 25.4-mm intracavity etalon. The calculation used a 2-ps time resolution.

based on the previously mentioned theory assuming that the etalon is tuned with all partial waves in phase and that the oscillator cavity condition is satisfied. The calculation was made with a 2-ps time resolution. The depth of modulation of the data in Fig. 53.28 is limited by the bandwidth of the measurement equipment.

To eliminate the temporal modulation shown in Fig. 53.28 a second intracavity etalon was used. Insertion of a 5-mm etalon in addition to the 25.4-mm etalon produced the output shown in Fig. 53.30 for the same experimental conditions. The envelope of the pulse in Fig. 53.30 shows the injected 70-ps-FWHM pulse stretched to 7-ns FWHM. Here the 7-ns pulse width is comparable to the 13-ns, laser-cavity round-trip time, and some pulse overlap effects can be seen between pulses in the pulse train. The corresponding theoretical calculation can also be seen in Fig. 53.30. For the calculation, 70 cavity round trips were assumed, which corresponded well with the measured cavity buildup time. Also used in the calculation was a 1.2-π phase shift per round trip in the cavity. (The laser-cavity length was not controlled, and hence, a constant phase shift with arbitrary value between 0 and 2π occurred every cavity round trip. The assumed 1.2-π phase shift per cavity round trip gave the best fit to the data.) Closer examination of the output pulse showed the temporal profile to be modulation free, both theoretically with 4-ps resolution and experimentally with the ~100-ps resolution limited by the bandwidth of the measurement equipment. We would expect no measurable modulation on even faster time scales; however, streak-camera measurements with higher temporal resolution are planned. The 7-ns pulse width was not limited and could, in principle, be stretched to any desired value.

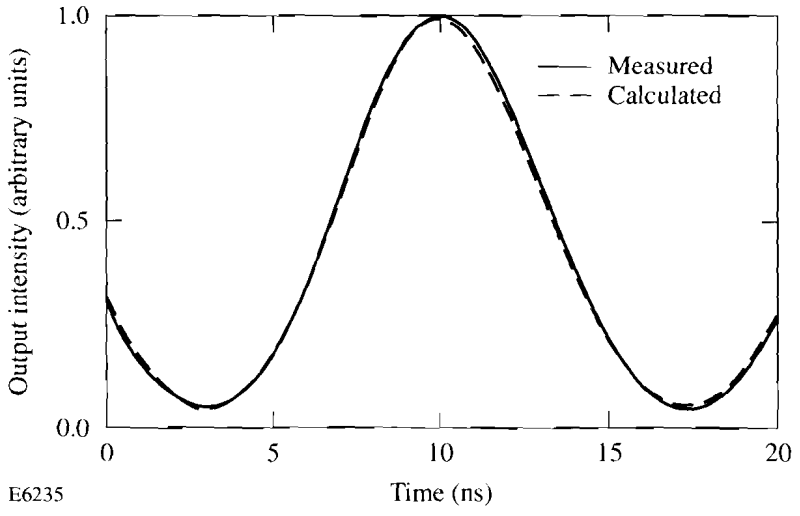

Fig. 53.30
The measured and calculated output-intensity temporal profiles of a regenerative amplifier with a 25.4-mm and a 5-mm intracavity etalon. The response time of the detection system was approximately 100 ps. The calculation used a 4-ps time resolution.

To produce repeatable laser output, the intracavity etalons were temperature stabilized and angle tuned to minimize the buildup time for the output pulse envelope. This corresponds to all partial waves of the etalons adding in phase to maximize the transmission of the etalon and minimize the intracavity losses. If

the etalon is not tuned in angle and temperature, the transmission of the etalon will be less than 100%. In that case, some of the power incident on the etalon will be reflected at an angle to the cavity lasing mode and blocked by an intracavity aperture. This would represent a loss to the laser cavity that would manifest itself as an increase in the laser buildup time. To test the temperature sensitivity of an intracavity etalon, the temperature of a 4-mm etalon was increased after it was angle tuned in the laser cavity. As the etalon temperature increased, the buildup time of the laser cavity increased to a certain value. As the temperature continued to increase, the buildup time began to decrease. After a temperature increase of approximately 12°C, the buildup time returned to its original value indicating that the etalon was tuned through one free spectral range. By decreasing the temperature to its original value, the process repeated itself in reverse and the buildup time again returned to its original value. This result agrees well with the calculated thermal sensitivity previously mentioned.

Implementation

Regenerative amplifiers have been installed in OMEGA with pulse-shaping capability.[3] A 70-ps-FWHM pulse from a cw mode-locked laser is injected into a regenerative amplifier. The system regen operates with a 4-mm-thick etalon with 50% reflective coatings on each surface. After the injected pulse makes approximately 40 round trips in the cavity, a 650-ps pulse is emitted. The etalon is housed in a copper block and is temperature controlled to 0.1°C. When pulses having a sharp rising edge are required, a 5-mm-thick etalon is inserted into the cavity producing approximately 1.3-ns pulses for the same conditions. These longer pulses are then shaped with a photoconductively switched Pockels cell.

The design of the GDL regens are similar to the OMEGA regens. In GDL the main-pulse laser will use an intracavity etalon with approximately 4-mm thickness. The timing scheme for GDL is simplified such that pulse-width control will be achieved by simply changing the buildup time (gain) of the regen, followed by moving the output pulse in time so as to be synchronous with the rest of GDL timing. This choice of etalon should allow a range of 500- to 1000-ps output pulse width. The foot-pulse regen will use two etalons having thicknesses of 5 mm and 25 mm, respectively. This combination of etalons should allow for temporally smooth pulses with approximately 5- to 6-ns pulse width. All etalons will be temperature controlled to within 0.1°C.

Summary

A regenerative amplifier with intracavity etalons has been analyzed and tested. The analysis is based on linear systems theory. The analysis can predict the output temporal profile of a regenerative amplifier given the input injected-pulse temporal profile and the details of the laser-cavity and intracavity etalons. The output temporal profile of the regenerative amplifier was measured as we varied the etalon thickness and the number of round trips that the injected pulse made in the laser cavity. Temporal modulation on the output pulse was calculated and observed for a single thick intracavity etalon. An injected pulse 70-ps wide was stretched to 7 ns with no temporal modulation using two etalons. The effect of raising the temperature of an etalon was also measured and analyzed. A 12°C change in the etalon temperature tuned the etalon through one free

spectral range as predicted by theory. Regenerative amplifiers having variable pulse widths have been implemented in OMEGA and GDL. All measurements agree well with the calculations made from that simple theory. This analysis lends itself to many other systems such as systems with resonant reflectors, multimirror cavities, etc. It can also be used for an injected pulse having an arbitrary temporal profile or phase modulation.

ACKNOWLEDGMENT

This work was supported by the U.S. Department of Energy Office of Inertial Confinement Fusion under Cooperative Agreement No. DE-FC03-92SF19460, the University of Rochester, and the New York State Energy Research and Development Authority. The support of DOE does not constitute an endorsement by DOE of the views expressed in this article.

REFERENCES

1. LLE Review **50**, 71 (1992).
2. M. D. Skeldon and S. T. Bui, to be published in the *Journal of the Optical Society of America B*.
3. M. D. Skeldon, S. T. Bui, S. Letzring, and W. Siryk, in *Solid State Lasers III*, edited by G. J. Quarles (SPIE, Bellingham, WA, 1992), Vol. 1627.
4. M. Born and E. Wolf, *Principles of Optics*, 5th ed. (Pergamon Press, Oxford, 1975).
5. J. D. Gaskill, *Linear Systems, Fourier Transforms, and Optics* (Wiley, New York, 1978).
6. A. Papoulis, *Systems and Transforms with Applications in Optics* (McGraw-Hill, New York, 1968), p. 379.
7. W. Koechner, *Solid-State Laser Engineering* (Springer-Verlag, New York, 1988), p. 218; "Fused silica," Technical Rep. (Corning, Inc., MP-21-4, Corning, NY, 14831).

1.F Shaping of Nanosecond Linearly Chirped Pulses

The importance of detailed laser pulse shapes in optical communications, ultrafast spectroscopy, and laser fusion has seen increasing recognition recently. Pulse shaping has traditionally been difficult to perform, and no approach has been entirely successful in achieving the goals of fast rise time, flexibility, stability, and contrast. Laser pulses have been shaped by performing techniques in time domain, frequency domain, or in a combination thereof.[1] Time-domain

pulse-shaping techniques, which include gain saturation (or saturable absorption), acousto-optic, and electro-optic techniques, have been proposed for certain temporal modulations. Frequency-domain pulse shaping,[2–11] which is accomplished by using diffraction gratings, has the capability of producing a wide range of picosecond and femtosecond pulse shapes and has been used in both optical communications and ultrafast spectroscopy.

In laser inertial-confinement fusion, relatively long pulses with detailed pulse shapes are required to influence the fusion capsule's implosion dynamics.[12] Useful pulse-shaping techniques should be able to provide both nanosecond pulses and flexible pulse shapes. Time-domain, electro-optical pulse-shaping techniques, which have long been studied, have difficulty achieving 100-ps response times and accurately controlled flexible pulse shapes. Frequency-domain pulse-shaping techniques (well known for their flexibility) therefore become the candidates for laser-fusion technological research.

Frequency-domain pulse shaping, however, is usually applied to ultrashort pulses where their relatively broad bandwidths allow for easy separation of the frequency components of the laser beam within a reasonable distance (~1 m).[5–11] In laser fusion, because of other requirements such as beam smoothing[13] and frequency conversion,[14] the laser bandwidth must often be carefully limited. The difficulty of stretching and shaping a narrow-band, ~60-ps laser pulse from a mode-locked oscillator to ~10 ns has limited the application of spectral pulse-shaping techniques in laser fusion.[4] Skupsky *et al.* recently proposed a spectral-beam-deflection, pulse-shaping scheme using an electro-optical device to encode the laser beam with phase-modulated bandwidth for spectral pulse shaping.[1] The advantage of this scheme is that after pulse shaping the laser beam can be sent into an inverse electro-optical device to remove the encoded phase modulation and narrow the bandwidth. This scheme would reduce the bandwidth concern of using spectral pulse shaping in laser fusion. However, appropriate electro-optical devices are not yet available for use in this application.

This article reports on the stretching and shaping of nanosecond linearly chirped pulses using an all-optical, passive, two-grating pulse-shaping system.[2–7] We focus on the temporal response of a linearly chirped pulse shaped by a unit-step spectral mask (a sharp edge at the spectral plane). The rise time is studied as a function of the laser bandwidth, frequency chirp, and the spectral resolution of the pulse-shaping system. We have also designed a lens system placed inside the two-grating pulse-shaping system to provide the large effective grating separation and control the spectral resolution for the shaping and stretching of narrow-band pulses. Laser pulses are originally generated from an Nd:YLF mode-locked oscillator. A single-mode optical fiber is used to produce the required bandwidth. These pulses are then sent to the passive two-grating system for stretching and shaping. The benefit of the passive pulse-shaping system is its simplicity, flexibility, and reproducibility. The bandwidth concern, associated with very fast rise-time applications, can be solved by using Skupsky's scheme[1] once the active electro-optical device is available for bandwidth generation and reduction.

Basic Equations

The fundamental frequency-domain pulse-shaping scheme was invented by E. B. Treacy in 1969.[2] Two parallel gratings were originally used for pulse compression or expansion. This scheme was later extended for pulse shaping by introducing a spectral mask and a retro-reflecting mirror after the grating pair.[3] Figure 53.31 shows a similar scheme with the use of transmission gratings operating in the Littrow configuration. The spectral angular dispersion Γ ($\equiv d\theta/d\lambda$) is generated when the laser beam passes through the first grating.

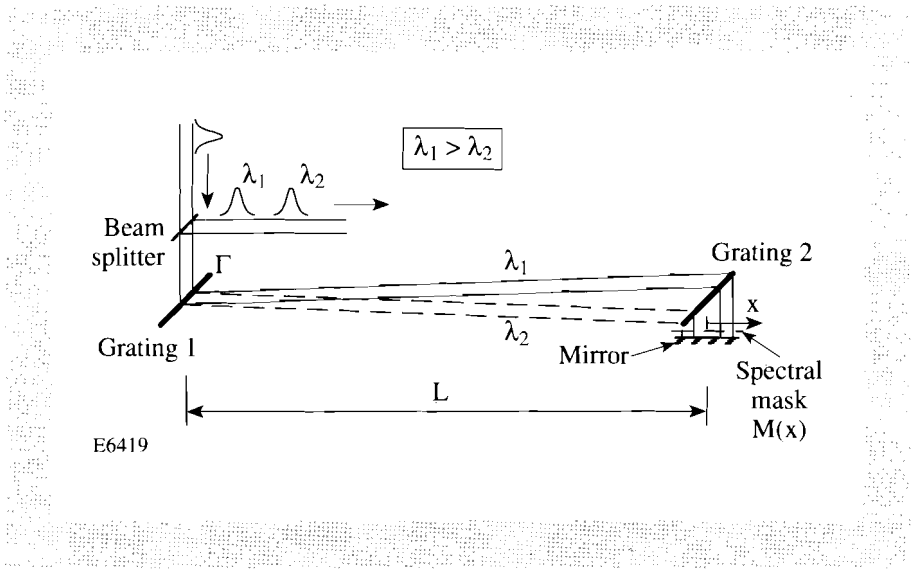

Fig. 53.31
The basic pulse-shaping and stretching scheme. Two representative waves λ_1 and λ_2 show the spectral dispersion and group delay.

After the dispersive laser beam propagates a distance L, its spectral angular dispersion is cancelled by the second grating, which has the same groove spacing as the first grating but an opposite incidence angle. The grating pair spatially separates the frequency components of the input laser pulse. The phase and/or amplitude of these spectral components are then modified by a spectral mask. Upon returning through the grating pair, these modified spectral components are recombined to form the desired pulse shape. Two representative waves λ_1 and λ_2 depict the spatial separation and group delay between different frequency components. Note that the distance traveled by the λ_1 component is longer than the distance traveled by the λ_2 component. This produces a linearly chirped pulse. Because of the linear relationship between frequency and time, a linearly chirped pulse can be shaped in the frequency domain and then mapped directly into the time domain.

The function of the two-grating pulse-shaping system shown in Fig. 53.31 can be expressed by one stretching function and one spectral-filtering function. The stretching function can be expressed as $\exp(ik_0L\beta^2\omega^2)$ in the frequency domain,[2] where ω is the frequency shift from the central frequency ω_0, k_0 is the wave vector at central frequency ω_0, L is the grating separation, and

$\beta \equiv d\theta/d\omega = -(\lambda^2/2\pi c)\Gamma$ describes the angular dispersion. The spectral-filter function for this system, with a Gaussian beam of waist w_o located at the spectral mask $M(x)$, is[7]

$$S(\omega) \equiv \sqrt{\frac{2}{\pi w_o^2}} \int_{-\infty}^{\infty} M(x) \exp\left[-2\left(x - \frac{dx}{d\omega}\omega\right)^2 / w_o^2\right] dx \,. \tag{1}$$

For the particular pulse-shaping scheme shown in Fig. 53.31, $dx/d\omega = \beta L$. If we consider only the frequency-dependent terms, we can write the stretched and shaped pulse as

$$E_{out}(\omega) = E_{in}(\omega) \exp\left(ik_o L\beta^2\omega^2\right) S(\omega) \,, \tag{2}$$

where $E_{in}(\omega)$ and $E_{out}(\omega)$ represent the input and output pulses in the frequency domain, respectively. Equations (1) and (2) are well studied in pulse compression and spectral pulse shaping. In this article we apply these two equations specifically to pulses with a large frequency chirp.

Spectral pulse shaping can be represented more intuitively by using the following three parameters: the length spanned by all frequency components on the spectral mask Δx; the group delay $\Delta\tau$ between the limiting spectral components; and the spectral resolution N. For a laser pulse with a bandwidth $\Delta\omega = -(2\pi c/\lambda^2)\Delta\lambda$ passed through the grating pair as shown in Fig. 53.31, the spatial separation of the frequency components can be understood by the simple geometric relation

$$\Delta x = \beta L \Delta\omega = \Gamma L \Delta\lambda \,. \tag{3}$$

This equation simply depicts the space-frequency relation $dx/d\omega = \beta L$ for Eq. (1). The group delay introduced by the system (round trip) is $4\Delta x \tan\theta/c$, where θ is the grating angle in the Littrow mode. By using Eq. (3) and $\beta \equiv d\theta/d\omega = 2\tan\theta/(k_o c)$, this group delay can be rewritten as $2k_o\beta^2 L\Delta\omega$. For an input chirped pulse $E_{in}(\omega) = A_{in}(\omega)\exp[i\phi_{in}(\omega)]$, where $A_{in}(\omega)$ and $\phi_{in}(\omega)$ are real functions, the total phase shift of the output shaped pulse shown in Eq. (2) is equal to

$$\phi(\omega) \equiv \phi_{in}(\omega) + k_o\beta^2 L\omega^2 \,,$$

and the total group delay of the output shaped pulse becomes[2]

$$\Delta\tau = \frac{d^2\phi(\omega)}{d\omega^2}\Delta\omega = \left[\frac{d^2\phi_{in}(\omega)}{d\omega^2} + 2k_o\beta^2 L\right]\Delta\omega \,. \tag{4}$$

The spectral resolution N is related to the the parameter Δx and is defined as[7]

$$N \equiv \Delta x / w_o \,, \tag{5}$$

where w_o is the Gaussian beam waist at the spectral mask. It is important to note that as the beam waist w_o approaches zero the spectral resolution approaches infinity, and the spectral filter function $S(\omega)$ approaches exactly the same shape as the spectral mask $M(x)$.

Unit-Step Spectral Filtering

To understand the space-frequency-time relationship in spectral pulse shaping, we focus on the case of a pulse with a large frequency chirp shaped by a sharp edge placed at the spectral plane; that is, shaped by a unit-step spectral mask

$$M(x) = \begin{cases} 0 & x < x_1 \\ 1 & x \geq x_1 \end{cases} . \tag{6}$$

The spectral filter function described by Eq. (1) can be solved as[7]

$$S(\omega) = \frac{1}{2}\left\{1 + erf\left[\sqrt{2}\left(\omega - \frac{\Delta\omega}{\Delta x} x_1\right) \Big/ \left(\frac{\Delta\omega}{N}\right)\right]\right\} , \tag{7}$$

where $\Delta\omega$ is the input laser bandwidth, N is the spectral resolution, and $\Delta\omega/\Delta x = 1/(\beta L)$ for the scheme shown in Fig. 53.31. The spectral filter function described by Eq. (7) is a smooth curve related to the error function. For an input pulse with a uniform spectrum across the sharp edge, the function $|S(\omega)|^2$ describes the shaped power spectrum near the sharp edge. The rising edge of the power spectrum spans a spectral width $\Delta\omega/N$. For the same spectral mask and the same input pulse, the shaped pulse described by Eq. (2) can be solved as

$$E_{out}(t) = \frac{1}{2}\exp\left[i\left(\omega_o t - \frac{2t^2}{\tau_{min}^2}\right)\right]\left\{1 + erf\left[e^{-i\frac{\alpha}{2}}\sqrt{2}\left(t - \frac{\Delta\tau}{\Delta x} x_1\right) \Big/ \tau_r\right]\right\} , \tag{8}$$

where *erf* is the complex error function and ω_o is the central frequency of the input laser. The time-space relation $\Delta\tau/\Delta x = [d^2\phi(\omega)/d\omega^2]/(dx/d\omega)$ can be obtained by combining Eqs. (3) and (4). The phase α is defined as

$$\alpha \equiv \tan^{-1}\left[\frac{4}{w_o^2}\left(\frac{dx}{d\omega}\right)^2 \Big/ \frac{d^2\phi(\omega)}{d\omega^2}\right] = \tan^{-1}\left(\frac{4N^2}{\Delta\omega\Delta\tau}\right) , \quad 0 \leq \alpha \leq \frac{\pi}{2} . \tag{9}$$

Later we will show that the parameter α is an indication of the intensity (energy) rippling of the shaped pulse. For an input transform-limited pulse, that is,

$\phi_{in}(\omega)=0$, the phase α can be simplified as $\alpha=\tan^{-1}(L/z_R)$, where L is the grating separation and $z_R=k_0 w_0^2/2$ is the Rayleigh range of the Gaussian beam. The two time constants τ_{min} and τ_r in Eq. (8) are defined as

$$\tau_{min} \equiv 2\sqrt{\frac{d^2\phi(\omega)}{d\omega^2}} = 2\sqrt{\frac{\Delta\tau}{\Delta\omega}}\ , \tag{10}$$

$$\tau_r \equiv \frac{\tau_{min}}{\sqrt{\sin\alpha}}\ . \tag{11}$$

The time constant τ_r can be treated approximately as the rise time of the shaped pulse, which is defined as the time required for the laser intensity to rise from 10% to 90% of its final value. (When α is small, the time constant τ_r is equal to 0.95 rise time, and when α approaches $\pi/2$, the time constant τ_r is equal to 96% of the rise time.) The time constant τ_{min} is the minimum rise time of the shaped pulse that can be obtained from the current pulse-shaping system. It is obvious from Eq. (11) that when the parameter α approaches $\pi/2$, the rise time τ_r approaches its minimum value τ_{min}. This time constant τ_{min} is also the shortest half pulse width (at e^{-1} amplitude point) of a Gaussian pulse that can be obtained by using a Gaussian spectral mask.[1] From Eq. (10) we know that the minimum rise time τ_{min} is proportional to the square root of the group delay per spectral width. Therefore, for a given group delay, the minimum rise time τ_{min} of the shaped pulse is determined by the input laser bandwidth $\Delta\omega$.

Figure 53.32 shows the unit-step-response curves of the laser intensity $|E_{out}(t)|^2$ with different values of tan α. When the spectral resolution N is large, the phase α approaches $\pi/2$ ($\tan\alpha \to \infty$) and the complex error function in Eq. (8) can be expressed by Fresnel integrals.[15] The temporal rippling of the shaped pulse in this case behaves exactly like Fresnel diffraction by a semi-infinite opaque screen. When the spectral resolution N is small, the phase α approaches zero, and the rippling disappears at the price of slower rise time. From Eqs. (9) and (11) we know that to reduce the temporal rippling (reduce α) we need to make a compromise with the rise time τ_r. When we choose $\alpha = \pi/4$ for Eq. (8), we find that the temporal rippling can be greatly reduced while the rise time τ_r does not increase significantly. This intensity response is shown by the thick solid curve in Fig. 53.32. We therefore apply tan $\alpha = 1$ to Eq. (9) and choose the optimal spectral resolution $N_{optimum}$ for the unit-step filtering system as

$$N_{optimum} = \frac{1}{2}\sqrt{\Delta\omega\Delta\tau}\ . \tag{12}$$

The easiest way to control the spectral resolution $N \equiv \Delta x/w_0$ is to adjust the size of the Gaussian beam waist w_0 on the spectral mask. Through the proper choice of the beam size on the spectral mask one can avoid the temporal rippling on the

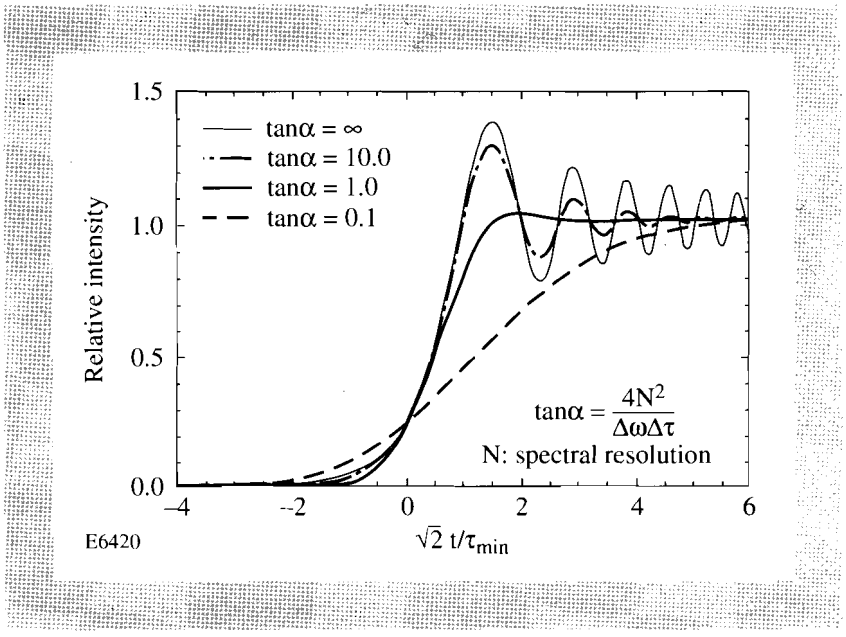

Fig. 53.32
The temporal-response curves of linearly chirped pulses shaped by a unit-step spectral mask. Limiting spectral resolution (thick solid line, tan $\alpha = 1$) can reduce the intensity rippling but still retain a good rise time.

shaped pulse without significant degradation of the rise time. Figure 53.32 also shows an important feature that at $t = 0$ the laser intensity rises to one quarter of its steady-state value and is independent of the parameter α. This was to be expected since half of the wavefront is obstructed by the spectral mask, the amplitude is halved, and the intensity drops to one quarter.

To obtain square pulses, one can immediately extend the previous unit-step spectral-filtering results to a square spectral window

$$M(x) = \begin{cases} 1 & x_1 \le x \le x_2 \\ 0 & \text{else} \end{cases} . \tag{13}$$

By applying Eq. (8) at $x = x_1$ and subtracting the unit-step response at $x = x_2$, the normalized laser intensity becomes

$$\left| E_{\text{out}}(t) \right|^2 = \frac{1}{4} \left| erf\left[e^{-i\frac{\alpha}{2}} \sqrt{2} \left(t - \frac{\Delta\tau}{\Delta x} x_1 \right) / \tau_r \right] - erf\left[e^{-i\frac{\alpha}{2}} \sqrt{2} \left(t - \frac{\Delta\tau}{\Delta x} x_2 \right) / \tau_r \right] \right|^2 . \tag{14}$$

Equation (14) shows that the time scales for both leading and trailing edges of the shaped pulse are equal to τ_r. As previously stated, one can adjust the spectral resolution N and the input laser bandwidth $\Delta\omega$ to obtain a square pulse with the desired rise time τ_r but without temporal rippling.

Schemes for Narrow-Bandwidth Pulses

Simple imaging systems can effectively provide the required grating separation for narrow-band pulses and at the same time control the laser-beam diffraction. Figure 53.33 schematically shows our first pulse-stretching-and-shaping system for narrow-band pulses, which consists of a pair of transmission gratings, a lens system including one down-collimator and one up-collimator, a spectral mask, and a retro-reflecting mirror. Four lenses with focal lengths f_1, f_2, f_3, and f_4 form the down-collimator and the up-collimator. Distances ℓ_1 to ℓ_6 describe the relative location of the optical elements. The spectral angular dispersion of the laser beam Γ ($\equiv d\theta/d\lambda$) is generated after passing through the first grating. The down-collimator magnifies the spectral angular dispersion from Γ to $M\Gamma$, where the magnification M is defined as

$$M \equiv -\frac{f_1}{f_2} = -\frac{f_4}{f_3} . \tag{15}$$

The up-collimator magnifies the spatial separation of different optical frequencies and returns the spectral angular dispersion from $M\Gamma$ back to Γ. The spectral angular dispersion is then cancelled by the second grating, which has the same groove spacing as the first grating but an opposite incidence angle. Two representative frequency components, denoted as λ_1 and λ_2, show the spectral

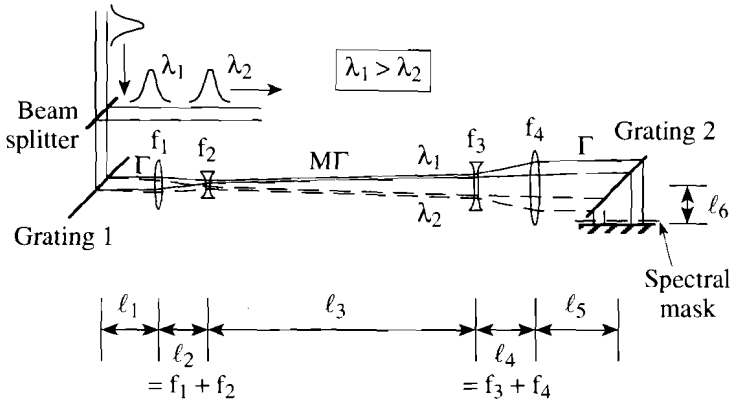

Effective grating separation: $L = M^2\ell_3 + M(f_1 + f_2 + f_3 + f_4) + \ell_1 + \ell_5$

E6421

Fig. 53.33

One down-collimator and one up-collimator effectively provide the required large effective grating separation. The down-collimator magnifies the spectral angular dispersion from Γ to $M\Gamma$. The up-collimator magnifies the spatial separation of different optical frequencies and returns the spectral angular dispersion from $M\Gamma$ back to Γ. The effective grating separation is $L = M^2\ell_3 + M(f_1 + f_2 + f_3 + f_4) + \ell_1 + \ell_5$, with $M \equiv -f_1/f_2 = -f_4/f_3$.

angular dispersion and the beam-size variation. Since the distance traveled by the λ_1 component is longer than the distance traveled by the λ_2 component, the output pulse will have a linear chirp.

The imaging system between the two gratings can be described by the well-known technique of ABCD matrices.[16] The ABCD matrices are developed from geometrical optics where an optical ray traveling a distance L is described by

$$\begin{bmatrix} x_2 \\ x_2' \end{bmatrix} = \begin{bmatrix} 1 & L \\ 0 & 1 \end{bmatrix} \begin{bmatrix} x_1 \\ x_1' \end{bmatrix},$$

and passing though a thin lens of focal length f is described by

$$\begin{bmatrix} x_2 \\ x_2' \end{bmatrix} = \begin{bmatrix} 1 & 0 \\ -1/f & 1 \end{bmatrix} \begin{bmatrix} x_1 \\ x_1' \end{bmatrix}.$$

The variables x_1 and x_2 are the input and output transverse displacements from the optical axis, and x_1' and x_2' are the slopes. In this manner we can obtain the spectral angular dispersion and the beam variation at the same time and can further apply the Huygen's integral to obtain the physical-optics results.[17] The ABCD matrix for the first optical system is obtained by writing the matrix for each component and distance and then multiplying. The result is

$$\begin{bmatrix} A & B \\ C & D \end{bmatrix}_I = \begin{bmatrix} 1 & L \\ 0 & 1 \end{bmatrix}, \tag{16}$$

where

$$L = M^2 \ell_3 + M(f_1 + f_2 + f_3 + f_4) + \ell_1 + \ell_5 \tag{17}$$

is the effective grating separation. Parameters ℓ_1, ℓ_3, and ℓ_5 represent the distances from the first grating to the down-collimator, from the down-collimator to the up-collimator, and from the up-collimator to the second grating, respectively. From Eq. (17) we know that the effective grating separation will be large if the magnification M is large.

Our second pulse-stretching-and-shaping system, shown schematically in Fig. 53.34, consists of the same optical components as the first system but with a somewhat more complicated arrangement, where $\ell_1 = f_1$, $\ell_2 = f_1 + f_2 + \Delta$, $\ell_4 = f_3 + f_4$. The laser beam leaving the first grating carries a spectral angular dispersion Γ. The first lens, which is placed at a distance $\ell_1 = f_1$ away from the first grating, cancels the spectral angular dispersion of the laser beam and makes all frequency components parallel to each other. Once these parallel frequency components pass the second lens (f_2) the spectral angular dispersion of the laser beam becomes $M\Gamma$ and is independent of the second lens position. We place the second lens at a distance $\ell_2 = f_1 + f_2 + \Delta$ away from the first lens. The small lens displacement Δ is used to control the beam diffraction and put the Gaussian beam

waist on the spectral mask $M(x)$. With this design the Fourier plane, which is formed by the beam waists of all frequency components, can be moved independently without affecting the spectral angular dispersion. The laser beam, after propagating a distance ℓ_3 away from the second lens, enters into a telescope formed by two lenses with focal lengths f_3 and f_4. This telescope, similar to the up-collimator in the first system, magnifies the spatial separation of different frequency components and returns the spectral angular dispersion from $M\Gamma$ back to Γ. The spectral angular dispersion is then cancelled by the second grating. The improvement of the spectral resolution caused by the displacement of the second lens can be understood by comparing the representative spectral components λ_1 and λ_2 in Figs. 53.33 and 53.34. Figure 53.34 shows a smaller Gaussian waist on the spectral mask for each frequency component.

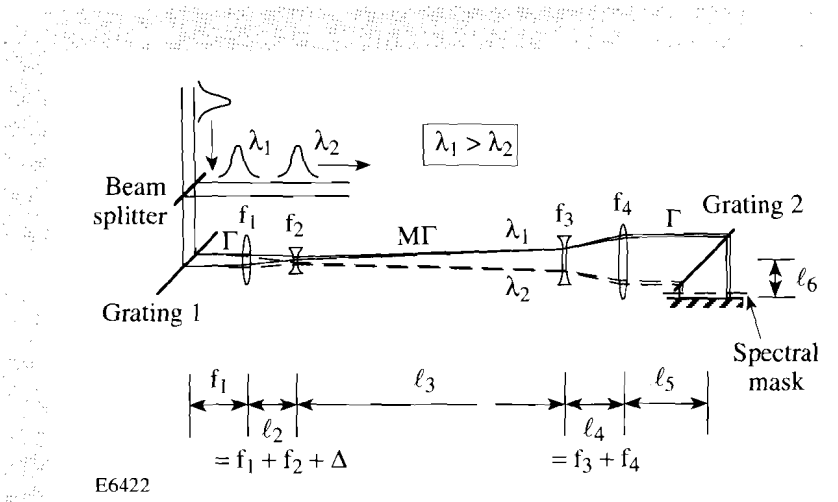

Fig. 53.34
The second spectral pulse-shaping scheme for narrow-band pulses: $\ell_1 = f_1$ and $\ell_2 = f_1 + f_2 + \Delta$. The second lens ($f_2$) is moved back a distance Δ to put the beam waist on the spectral mask. The spectral angular dispersion of the laser beam leaving the second lens is magnified to $M\Gamma$ and is independent of the second lens position.

The ABCD matrix for the second optical system is

$$\begin{bmatrix} A & B \\ C & D \end{bmatrix}_{II} = \begin{bmatrix} 1 - \dfrac{\Delta}{f_1^2} L & L \\ -\dfrac{\Delta}{f_1^2} & 1 \end{bmatrix} \tag{18}$$

The effective grating separation becomes

$$L = M^2 \ell_3 + M(f_1 + f_3 + f_4) + \ell_5 \,. \tag{19}$$

From $\ell_1 = f_1 = -Mf_2$ we know that Eqs. (17) and (19) are similar. The second optical system can also provide large effective grating separation if the magnitude of the parameter M is large. The ABCD matrix in Eq. (18) can be decomposed as

$$\begin{bmatrix} 1-\dfrac{\Delta}{f_1^2}L & L \\ -\dfrac{\Delta}{f_1^2} & 1 \end{bmatrix} = \begin{bmatrix} 1 & L \\ 0 & 1 \end{bmatrix} \begin{bmatrix} 1 & 0 \\ -\dfrac{\Delta}{f_1^2} & 1 \end{bmatrix}.$$

This is equivalent to a laser beam passing a lens with a focal length f_1^2/Δ and propagating a distance L.

We now apply the Gaussian beam analysis to our spectral pulse-shaping system as if the gratings were really separated a distance L.[17] For a collimated input beam, the second system can achieve significantly greater spectral resolution than the first. The axial position of the Gaussian beam waist of each frequency component in the second system is determined by the parameter Δ. To set the Gaussian waist on the spectral mask for a collimated input laser beam, the parameter Δ should be

$$\Delta = \frac{z f_1^2}{z^2 + z_R^2}, \tag{20}$$

where $z = L + \ell_6$ is the effective grating separation plus the distance from the second grating to the spectral mask, and $z_R \equiv k_0 w_0^2/2$ is the Rayleigh range of the Gaussian beam near the spectral mask. Equation (20) is obtained by matching the wavefront radius of curvature $z + z_R^2/z$ (see Ref. 16) to the overall focal length of the system f_1^2/Δ [Eq. (18)]. The relation between the input-beam size w_1 and the spot size on the spectral mask w_0 can be obtained from a Gaussian beam analysis

$$w_1 = w_0 \sqrt{1 + \frac{z^2}{z_R^2}}. \tag{21}$$

The spectral resolution of the system is limited by the laser-beam diffraction. For an input Gaussian beam with a beam waist w_1 at the first grating (collimated beam), the far-field diffraction half-angle is $\theta_d \equiv \lambda/\pi w_1$.[16] When the laser beam passes through the first grating, a spectral dispersion angle $\theta_\lambda \equiv \Gamma\Delta\lambda$ is added to the laser beam. To obtain the best spectral resolution we relay the Gaussian beam waist to the spectral mask where the beam waist $w_0 \approx \lambda L/\pi w_1 = \theta_d L$ [the limiting case $z >> z_R$ for Eq. (21)]. In this case the spectral resolution $N = \Gamma\Delta\lambda L/w_0$ approaches its maximum

$$N_{\max} = \frac{\theta_\lambda}{\theta_d}. \tag{22}$$

To increase the spectral resolution, one needs to increase the spectral dispersion angle θ_λ or decrease the diffraction angle θ_d. Increasing the grating angular dispersion Γ and the laser bandwidth $\Delta\lambda$ increases θ_λ. Increase of the input-beam size w_1 reduces θ_d. The input beam size w_1 is limited by the diameter of the first grating.

The system shown in Fig. 53.34 employs a novel way to obtain large group delay and high spectral resolution for narrow-band pulses. Figure 53.35 shows a multi-grating, folded-beam scheme in which a large group delay can be obtained with commonly available grating sizes. Two gratings in 67.5° Littrow mode are used as an example. The optical path traveled by the λ_1 component (solid line) is longer than that of the λ_2 component (dotted line) by an amount $16 D_2 \sin\theta$, where D_2 is the clear aperture of the second grating. For gratings with clear aperture $D_2 = 20$ cm, the optical path difference between λ_1 and λ_2 is about 3 m, which is equivalent to a 10-ns group delay. This grating arrangement can be used to replace the second grating in Fig. 53.34 to produce four-fold increase in the group delay. The spectral resolution can also be increased by a factor of 4 by replacing the first grating in Fig. 53.34 with the same grating arrangement as shown in Fig. 53.35, but with an opposite incidence angle.

The pulse-shaping systems described previously can provide large group delay and high spectral resolution for narrow-band pulses, though the pulse-shaping ability of the system is still limited by the laser bandwidth. From the unit-

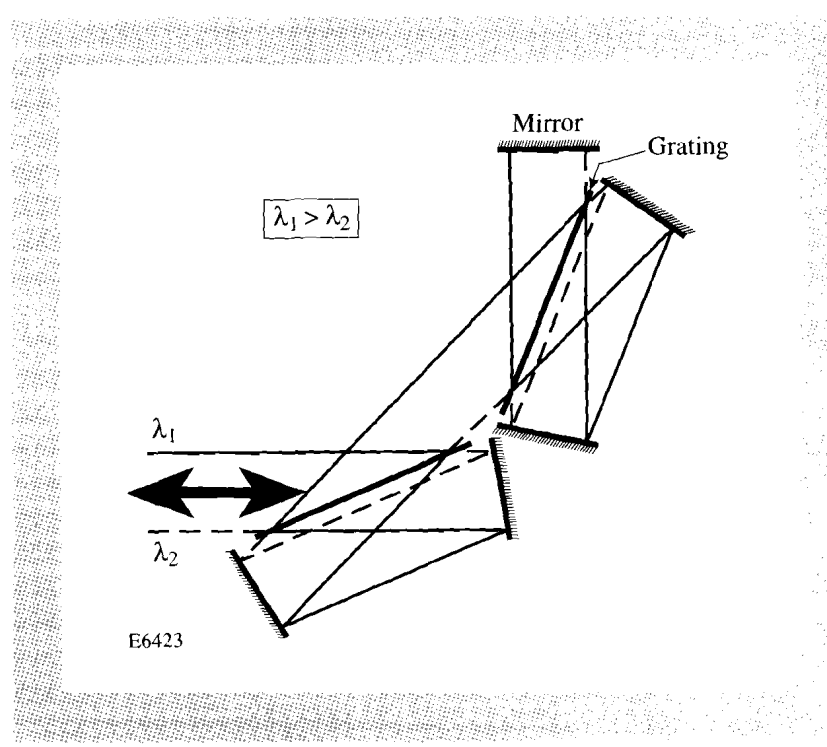

Fig. 53.35
A multi-grating, folded-beam scheme provides a large group delay with available grating sizes.

step-response analysis we know that the fidelity of the mapping from the spectral mask to the temporal pulse shape is determined by the minimum response time $\tau_{min} = 2(\Delta\tau/\Delta\omega)^{1/2}$. High spectral resolution allows the rise time τ_r to approach the minimum response time τ_{min}. However, the laser bandwidth $\Delta\omega$ must be large enough, for a given group delay $\Delta\tau$, to decrease τ_{min} to the desired amount.

Experiment

The purpose of this experiment was first to show the rise time and the flexibility of the spectral pulse-shaping technique and, secondly, to demonstrate the feasibility of the scheme for narrow-bandwidth pulses. The experimental setup follows the two-grating pulse-shaping scheme shown in Fig. 53.31. For shaping narrow-band pulses, the lens system shown in Fig. 53.34 was used to provide a large effective grating separation.

Figure 53.36 shows the details of the experimental setup for narrow-band pulses. A cw-pumped, mode-locked, Nd:YLF oscillator generates a 76-MHz train of ~77-ps pulses at a wavelength of 1053 nm. These pulses are coupled into a 2-km, single-mode optical fiber to generate the required bandwidth. Because of self-phase modulation and group-velocity dispersion occurring in the fiber, these pulses leaving the fiber can have a pulse width up to 240 ps and a bandwidth up to 30 Å. This bandwidth is wide enough for us to accurately study the minimum rise time of the shaped pulse versus the input laser bandwidth as described in Eq. (10). A 50% beam splitter transmits the input laser pulses and picks up the shaped pulses, which are sent back from the two-grating pulse-shaping system. The input laser beam, before entering the two-grating system, is collimated to different input beam sizes for different experimental conditions. The returned 2-mm laser beam, picked off by the beam splitter, is focused by a 200-mm focal-length lens into a 200-μm pinhole before entering into the streak camera. The spatial filtering reduces the effects of optical aberrations and ghost reflections that cause temporal modulation because of the interference effects from the space-to-time mapping. The time resolution of the streak camera used to measure the shaped pulse is ~14 ps.

The two-grating system shown in Fig. 53.36 is specifically for narrow-bandwidth pulses. Behind each grating two mirrors are used to double the angular dispersion and the group delay. The equivalent grating position of this folded-beam design is located midway between the two mirrors. Two transmission gratings are operated at 67.5° Littrow configuration. Both gratings have a 6-in. clear aperture and were holographically made using a new interferometric scheme.[18,19] The focal lengths of the lenses are $f_1 = f_4 = 600$ mm and $f_2 = f_3 = 80$ mm. For our convenience we have used positive focal lengths f_2 and f_3. Two turning mirrors are mounted on an optical rail and are used to adjust the optical path length between the f_2 lens and the f_3 lens (i.e., ℓ_3). The effective grating separation L described by Eq. (19) can be easily varied by shifting these two turning mirrors.

When aligning the f_1 lens, a retro-reflecting mirror is temporarily placed at the back focus of the f_1 lens. This mirror reflects the laser beam back to the beam splitter and the streak camera. The distance between the first grating and the f_1

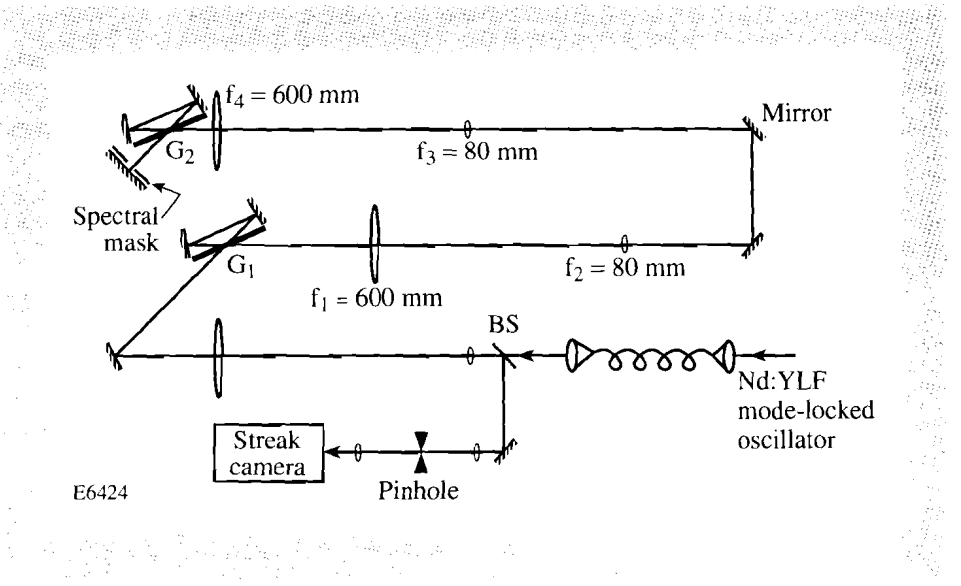

Fig. 53.36
Experimental setup for narrow-band pulses. BS: beam splitter; G_1 and G_2: transmission gratings.

lens is determined when no transverse-frequency chirp can be seen using the streak camera. The distance between the f_3 lens and the f_4 lens is accurately set using shearing interferometry. The second grating angle is carefully adjusted such that no transverse-frequency chirp can be seen using the streak camera. The fine adjustment of the f_2 lens position moves the Fourier plane to the spectral mask. We use an adjustable aperture (iris) in front of the system's retro-reflecting mirror as a binary spectral window to obtain square pulses. When shaping broad-bandwidth pulses, both the lenses inside the grating pair and the mirrors behind the gratings are removed, since the required grating separation is just several meters. The two-grating system is then like the one shown in Fig. 53.31.

Simple experiments and calculations demonstrate the performance of the spectral pulse-shaping system. Table 53.I shows the measured and calculated rise times of the stretched and shaped pulses under different frequency-chirp conditions: $\Delta\lambda/\Delta\tau = 20$ Å/ns, 5 Å/ns, 1 Å/ns, 0.61 Å/ns, and 0.13 Å/ns. In order to obtain this wide range of frequency chirp it is necessary to modify the two-grating setup in Fig. 53.36 to provide the required grating separation. For $\Delta\lambda/\Delta\tau = 20$ Å/ns, the lenses between the gratings and the mirrors behind each grating in Fig. 53.36 are removed. For $\Delta\lambda/\Delta\tau = 5.0$ Å/ns, the two mirrors behind each grating are installed to double the angular dispersion and shorten the required grating separation. For $\Delta\lambda/\Delta\tau = 1.0$ Å/ns and 0.61 Å/ns, the lens system is placed inside the grating pair as shown in Fig. 53.36, but the two mirrors behind each grating are removed. For $\Delta\lambda/\Delta\tau = 0.13$ Å/ns, the experimental setup is the same as in Fig. 53.36. The effective grating separations for the narrow-band cases, $\Delta\lambda/\Delta\tau = 1.0$ Å/ns, 0.61 Å/ns, and 0.13 Å/ns, are calculated from Eq. (19). The width of the spectral window $x_2 - x_1$ is adjusted so that a shaped pulse width of 1-ns (FWHM) is obtained. In each case, the spectral resolution is adjusted to

the optimal value [Eq. (12)] by controlling the beam waist w_0. The minimum rise time τ_{min} and the rise time τ_r at $\alpha = \pi/4$ are calculated from Eqs. (10) and (11), respectively. Table 53.I shows that the measured rise times are well located between the calculated minimum rise times τ_{min} and the estimated rise times τ_r.

Table 53.I: Measured and calculated rise times in different experimental conditions.

$\Delta\lambda/\Delta\tau$ (Å/ns)	Measured rise time (ps)	τ_{min} (ps)	τ_r ($\alpha = \pi/4$) (ps)	Two-grating system	L (m)	$x_2 - x_1$ (mm)	w_0 (mm)
20	34±7	34	40	No imaging No folding	4.2	38	2
5.0	78±7	68	81	No imaging Folded beam	4.36	17	1.5
1.0	175±11	153	182	With imaging No folding	67.5	35	5
0.61	201±11	198	236	With imaging No folding	111	35	6
0.13	501±30	424	505	With imaging Folded beam	132	20	7

E6533

Figure 53.37 shows experimental (solid lines) and calculated (dotted lines) pulse shapes of the stretched and shaped pulses for cases (a) 20 Å/ns, (b) 5 Å/ns, (c) 1 Å/ns, and (d) 0.13 Å/ns. The theoretical curves are obtained from numerically solving Eqs. (1) and (2) and are further checked against Eq. (8). The parameters $L, x_2 - x_1$, and w_0, used in this calculation, are listed in Table 53.I. In all cases, the rising (or trailing) edges of both theoretical curves and experimental results are very well matched.

The intensity (energy) noise near the peak of each experimental curve does not randomly vary during the course of many measurements. It was found to be fixed and different for each experimental setup. The noise is produced from several sources. The defects on the second grating affect the diffraction efficiency for each frequency component of the laser beam and imprint the noise on the output-shaped pulse. This noise can be identified by moving the grating such that the noise pattern changes as the grating moves. Also, etalon effects produced from transmission gratings and other optics cause beat patterns on top of the linearly chirped pulse.[4] Wedged optics should be used in shaping of linearly chirped pulses. In addition, lens aberrations can change the characteristics of the laser-beam waist on the Fourier plane and affect the shaped pulse. This noise can be reduced by spatially filtering the shaped laser beam. Each of these sources of noise can be eliminated with higher quality optical elements.

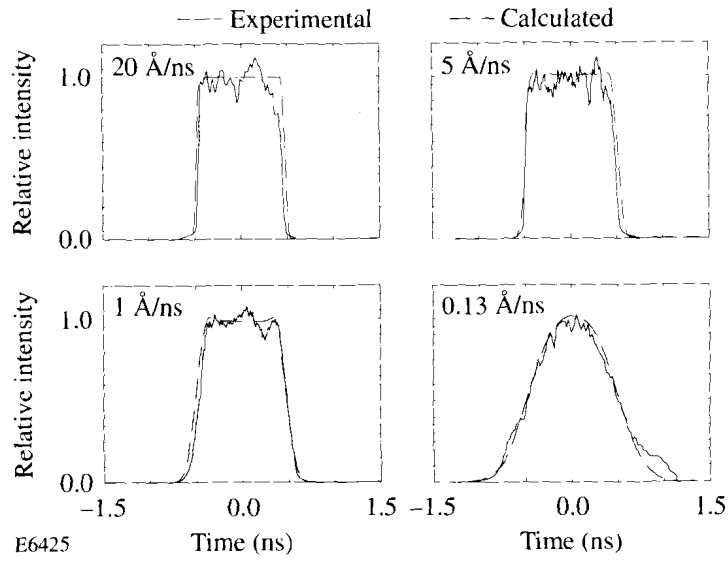

Fig. 53.37
Experimental (solid lines) and calculated (dotted lines) results of the stretched and shaped pulses under different frequency-chirp conditions: (a) 20 Å/ns, (b) 5 Å/ns, (c) 1 Å/ns, and (d) 0.13 Å/ns. The measured rise times are (a) 34 ps, (b) 78 ps, (c) 175 ps, and (d) 501 ps.

To show the flexibility of the spectral pulse-shaping technique we present the two shaped pulses shown in Fig. 53.38. The experimental setup is that shown in Fig. 53.36 without modification. The experimental parameters are $L = 27$ m and $w_0 = 1$ mm. The frequency chirp is 0.6 Å/ns. These two pulses are arbitrarily shaped using a simple binary mask in the spectral plane. The flexibility of this technique is currently limited by the availability of masks with variable-gray levels. However, from this simple demonstration we can infer that the spectral pulse-shaping technique is capable of producing a wide range of pulse shapes. System flexibility is important for later studies, using the OMEGA Upgrade, of how target performance is affected by laser pulse shapes.

Conclusion

This article has reported on all optical techniques for shaping and stretching nanosecond linearly chirped pulses. The fidelity of the mapping from the spectral mask to the temporal pulse shape for a linearly chirped pulse has been shown to be dependent on the laser bandwidth, the frequency chirp, and the spectral resolution. Proper design of these parameters leads to fast rise times and stable, smooth pulse shapes. A pulse-stretching scheme for narrow-band pulses was also presented and tested in this study. This spectral pulse-shaping technique provides the required stability, flexibility, and fast rise times necessary for laser-fusion research. Future investigation will include the injection of shaped pulses

into a regenerative amplifier, the generation of linearly chirped pulses from electro-optical modulators, the use of a zero-dispersion pulse-shaping scheme, and the deployment of a liquid-crystal, spectral-light modulator for flexible mask generation.

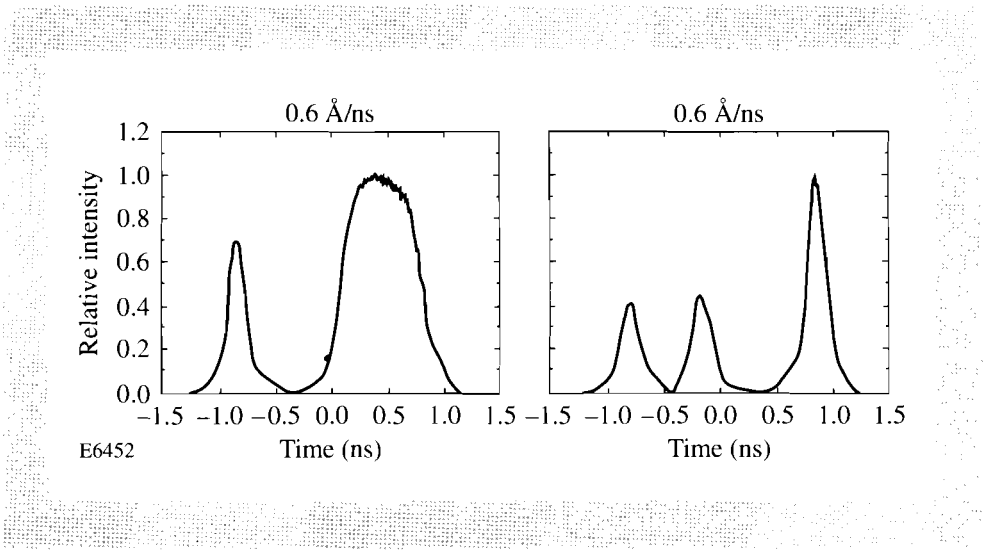

Fig. 53.38
Simple examples of shaped pulses showing the spectral pulse-shaping technique capable of producing a wide range of pulse shapes. The frequency chirp is 0.6 Å/ns for both cases.

ACKNOWLEDGMENT

The authors would like to thank J. Armstrong for providing the transmission gratings and C. Kellogg for his assistance. This work was supported by the U.S. Department of Energy Office of Inertial Confinement Fusion under Cooperative Agreement No. DE-FC03-92SF19460, the University of Rochester, and the New York State Energy Research and Development Authority. The support of DOE does not constitute an endorsement by DOE of the views expressed in this article.

REFERENCES

1. S. Skupsky, T. Kessler, S. Letzring, and Y.-H. Chuang, submitted to the Journal of Applied Physics.
2. E. B. Treacy, IEEE J. Quantum Electron. **5**, 454 (1969).
3. J. Desbois, F. Gires, and P. Tournois, IEEE J. Quantum Electron. **9**, 213 (1973).
4. J. Agostinelli *et al.*, Appl. Opt. **18**, 2500 (1979).
5. J. P. Heritage, A. M. Weiner, and R. N. Thurston, Opt. Lett. **10**, 609 (1985).
6. A. M. Weiner, J. P. Heritage, and R. N. Thurston, Opt. Lett. **11**, 153 (1986).
7. R. N. Thurston *et al.*, IEEE J. Quantum Electron. **22**, 682 (1986).
8. O. E. Martinez, J. P. Gordon, and R. L. Fork, J. Opt. Soc. Am. A **1**, 1003 (1984).
9. O. E. Martinez, IEEE J. Quantum Electron. **23**, 59 (1987).

10. O. E. Martinez, IEEE J. Quantum Electron. **24**, 2530 (1988).

11. A. M. Weiner *et al.*, IEEE J. Quantum Electron. **28**, 908 (1992).

12. LLE Review **39**, 114 (1989).

13. S. Skupsky, R. W. Short, T. Kessler, R. S. Craxton, S. Letzring, and J. M. Soures, J. Appl. Phys. **66**, 3456 (1989).

14. R. S. Craxton, IEEE J. Quantum Electron. **17**, 1771 (1981).

15. *Handbook of Mathematical Functions with Formulas, Graphs, and Mathematical Tables*, edited by M. Abramowitz and I. A. Stegun (Dover, NY, 1970), p. 301; $erf\left[\left(\sqrt{\pi}/2\right)(1-i)z\right] = (1-i)\left[C(z) + iS(z)\right]$, where $C(z)$ and $S(z)$ are Fresnel integrals.

16. A. E. Siegman, *Lasers* (University Science, Mill Valley, CA, 1986), Chaps. 15–17, 20, and 21.

17. Y.-H. Chuang, T. J. Kessler, S. Skupsky, and D. L. Brown, submitted to the IEEE Journal of Quantum Electronics.

18. J. J. Armstrong, Masters thesis, University of Rochester (1992).

19. LLE Review **50**, 61 (1992).

Section 2
NATIONAL LASER USERS FACILITY NEWS

The first quarter of FY93 activity supported experiments from five NLUF users. Experiments from **H. Griem** (University of Maryland), **C. Hooper** (University of Florida), **J. Seely/U. Feldman** [Naval Research Laboratory (NRL)], **K. Mizuno/P. Drake** (Plasma Physics Research Institute), and **A. Honig** (Syracuse University) were scheduled and fielded on the OMEGA laser system. These experiments were scheduled as both dedicated laser time (A. Honig, H. Griem, and C. Hooper) and shots interleaved with LLE target shots (J. Seely and K. Mizuno). Instrumentation for these experiments was provided by the experimenters and by LLE.

H. Griem and **J. Moreno** from the University of Maryland completed their shots to study x-ray and XUV spectroscopy from high-density implosions. The targets used for this experiment were spherical plastic shells filled with Ne and D_2/Ne mixtures. Time-dependent line emission was measured with SPEAXS and a streak camera with a variable-space grating before the entrance slit. The proposed experiment was to measure the details of the line shapes as a function of core density.

C. Hooper did a similar series of experiments with Ar- and D_2/Ar-filled plastic shells. SPEAXS and a flat-crystal spectrograph built by NRL coupled to a streak camera were used to measure the time-dependent x-ray line shape of the Ar *k*-shell emission. These data are being analyzed by the group at the University of Florida and **P. Jaanimagi** at LLE.

J. Seely and U. Feldman developed two instruments and fielded a series of experiments using Xe- and Xe/D_2-filled plastic shells. A high-resolution flat-crystal spectrograph was developed as a front end for a large-format x-ray streak camera. The high resolution was needed to measure the time-dependent line spectroscopy of the xenon *L*-shell emission from imploded targets. This work was done in collaboration with scientists from LLNL and used a diagnostic that will be used for OMEGA Upgrade target implosions. This group has also developed a high-resolution Cassegrain XUV microscope. The instrument resolution was measured at two magnifications with Kodak 101 and Kodak 104 films.

K. Mizuno and P. Drake continued the development of a diagnostic to measure Thompson scattering from the ion-acoustic decay instability. This experiment used the long-scale-length plasmas generated on the OMEGA laser for plasma-interaction experiments. One OMEGA beam was used as the Thompson scattering probe beam. Time-dependent optical and UV spectroscopy was used to characterize the plasma and measure the scattered light.

A. Honig continued his development of a cryogenic target-handling system. This effort is needed for his research into fusion of spin-polarized HD and D_2 targets.

ACKNOWLEDGEMENT

This work was supported by the U.S. Department of Energy Office of Inertial Confinement Fusion under agreement No. DE-FC03-92SF19460.

Section 3
LASER SYSTEM REPORT

3.A GDL Facility Report

The refurbishment of the GDL facility, managed by **J. Kelly**, continued during the first quarter of FY93. This work will continue through the summer of 1993. Remodeling of the laser room, target room, and power-conditioning room has been completed. The tables needed to mount the laser system are in place and the laser hardware is being installed. The current OMEGA target chamber will be used as the new GDL target chamber. It will be installed during the second quarter of FY93.

3.B OMEGA Facility Report

The OMEGA laser facility fired a total of 528 shots during the first quarter of FY93. These shots were divided among driver-line, target-irradiation, laser-system, and software-test shots. The last shot on the current OMEGA laser system was taken 18 December 1992 at 17:08. The system is now shut down to begin the construction needed for the OMEGA Upgrade system.

The 282 target shots during this period included long-scale-length plasma interactions, induced, low-order, l-mode illumination asymmetrical implosions, measurement of the burnthrough time of plastic ablation layers (ablation layer-stability characterization), and five NLUF projects. These experiments were done with both Gaussian pulses and pulses with fast rise times.

The shot summary for the OMEGA laser this quarter is as follows:

Driver line		166
Laser system		68
Software tests		12
Target shots		282
	TOTAL	528

ACKNOWLEDGEMENT

This work was supported by the U.S. Department of Energy Office of Inertial Confinement Fusion under Cooperative Agreement No. DE-FC03-92SF19460, the University of Rochester, and the New York State Energy Research and Development Authority. The support of DOE does not constitute an endorsement by DOE of the views expressed in this article.

PUBLICATIONS AND CONFERENCE PRESENTATIONS

Publications

S. Alexandrou, R. Sobolewski, and T. Y. Hsiang, "Time-Domain Characterization of Bent Coplanar Waveguides," IEEE J. Quantum Electron. **28**, 2325 (1992).

D. K. Bradley, P. M. Bell, J. D. Kilkenny, R. Hanks, O. Landen, P. W. McKenty, P. A. Jaanimagi, and C. P. Verdon, "High-Speed Gated X-Ray Imaging for ICF Target Experiments," Rev. Sci. Instrum. **63**, 4813 (1992).

S. Y. Chou, Y. Liu, W. Khalil, M. I. Nathan, T. Y. Hsiang, and S. Alexandrou, "Ultrafast Nanoscale Metal-Semiconductor-Metal Photodetectors on Bulk and Low-Temperature-Grown GaAs," Appl. Phys. Lett. **61**, 819 (1992).

E. M. Epperlein, "Laser Filamentation in Plasmas," in *Research Trends in Physics: Inertial Confinement Fusion*, edited by K. A. Brueckner, N. G. Basov, S. W. Haan, and C. Yamanaka (AIP, New York, 1992), pp. 262–276.

P. M. Fauchet and T. Gong, "Femtosecond Dynamics of Hot Carriers in GaAs," in *Ultrafast Laser Probe Phenomena in Semiconductors and Superconductors*, edited by R. R. Alfano (SPIE, Bellingham, WA, 1992), Vol. 1677, p. 25.

B. S. W. Kuo, J. C. M. Li, and A. W. Schmid, "Thermal Conductivity and Interface Thermal Resistance of Si Film on Si Substrate Determined by Photothermal Displacement Interferometry," Appl. Phys. A **55**, 289 (1992).

F. J. Marshall, J. G. Jernigan, T. Collins, J. F. Arens, and G. Pien, "Measuring Laser-Plasma X-Ray Emission Using Photodiode Arrays," Rev. Sci Instrum. **63**, 5094 (1992).

C. I. Moore, "Confinement of Electrons to the Center of a Laser Focus via the Ponderomotive Potential," Journal of Modern Optics **39**, 2171 (1992).

Forthcoming Publications

P. S. Maruthi Sai, M. J. Levene, T. Gillbro, R. S. Knox, R. H. Hwang-Schweitzer, and S. Mahajan, "Time-Resolved Fluorescence of Phycoerythrocyanin-Containing Phycobilisomes from the Cyanobacterium Westiellopsis Prolifica," to be published in *Biophysical Journal*.

R. L. McCrory, J. M. Soures, J. P. Knauer, S. A. Letzring, F. J. Marshall, S. Skupsky, W. Seka, C. P. Verdon, D. K. Bradley, R. S. Craxton, J. A. Delettrez, R. Epstein, P. A. Jaanimagi, R. L. Keck, T. J. Kessler, H. Kim, R. L. Kremens, P. W McKenty, R. W. Short, and B. Yaakobi, "Short-Wavelength-Laser Requirements for Direct-Drive Ignition and Gain," to be published in *Lasers and Particle Beams*.

R. L. McCrory, R. E. Bahr, D. K. Bradley, D. L. Brown, R. S. Craxton, J. Delettrez, R. Epstein, P. A. Jaanimagi, T. Kessler, J. P. Knauer, S. Letzring, F. Marshall, P. W. McKenty, W. Seka, S. Skupsky, J. M. Soures, C. P. Verdon, and B. Yaakobi, "Direct-Drive Implosion Experiments for Laser Fusion on OMEGA and the OMEGA Upgrade," to be published in *Lasers and Particle Beams*.

R. L. McCrory, J. M. Soures, C. P. Verdon, T. R. Boehly, D. K. Bradley, R. S. Craxton, J. A. Delettrez, R. Epstein, R. J. Hutchison, P. A. Jaanimagi, S. D. Jacobs, J. H. Kelly, R. L. Keck, T. J. Kessler, H. Kim, J. P. Knauer, R. L. Kremens, S. A. Kumpan, S. A. Letzring, F. J. Marshall, P. W. McKenty, S. F. B. Morse, W. Seka, R. W. Short, M. D. Skeldon, S. Skupsky, and B. Yaakobi, "Direct-Drive Laser Fusion Target Physics Experiments," to be published in the *Proceedings of the 14th International Atomic Energy Agency (IAEA) International Conference on Plasma Physics and Controlled Nuclear Fusion Research*, Wurzburg, Germany, 30 September–7 October 1992.

R. L. McCrory, "Laser-Driven ICF Experiments," to be published in *Nuclear Fusion by Inertial Confinement*.

R. L. McCrory, "Direct-Drive Implosion Experiments for Laser Fusion on OMEGA and the OMEGA Upgrade," to be published in the *Proceedings of the 21st ECLIM*, Warsaw, Poland, 21–25 October 1991.

R. L. McCrory, "Irradiation Uniformity Requirements for Direct-Drive Laser Fusion," to be published in the *SPIE Proceedings of the XIV International Conference on Coherent and Nonlinear Optics*, St. Petersburg, Russia, 24–27 September 1991.

C. J. McKinstrie and M. V. Goldman, "Three-Dimensional Instabilities of Counterpropagating Light Waves in Homogeneous Plasmas," to be published in the *Journal of the Optical Society of America B*.

C. J. McKinstrie and X. D. Cao, "The Nonlinear Detuning of Three-Wave Interactions," to be published in the *Journal of the Optical Society of America B*.

D. D. Meyerhofer, H. Chen, J. A. Delettrez, B. Soom, S. Uchida, and B. Yaakobi, "Resonance Absorption in High Intensity Contrast, Picosecond Laser-Plasma Interactions," to be published in *Physics of Fluids*.

J. Peatross, B. Buerke, and D. D. Meyerhofer, "Sequential Ionization in ^{3}He with a 1.5 ps, 1-mm Laser Pulse," to be published in *Physical Review A*.

J. K. Samarabandu, R. Acharya, C. D. Edirisinghe, P. C. Cheng, H. Kim, T. H. Lin, R. G. Summers, and C. E. Musial, "Analysis of Multi-Dimensional Confocal Images," to be published in the *Proceedings of the SPIE Symposium "Biomedical Imaging,"* San Diego, CA, 24 February 1991.

N. Sampat, "Imaging System Design and Image Analysis Techniques for the Automatic Alignment of a Fusion Laser," to be published in the *Journal of Electronic Imaging.*

M. D. Skeldon and S. T. Bui, "The Temporal Mode Structure of a Regenerative Amplifier with Intracavity Etalons," to be published in the *Journal of the Optical Society of America B.*

S. Skupsky, T. J. Kessler, S. A. Letzring, and Y.-H. Chuang, "Laser-Beam Pulse Shaping Using Spectral Beam Deflection," to be published in the *Journal of Applied Physics.*

R. Sobolewski, W. Xiong, and W. Kula, "Patterning of Thin-Film, High-T_c Circuits by the Laser-Writing Method," to be published in *IEEE Transactions on Applied Superconductivity.*

R. Sobolewski, "Electro-Optic Time Domain Characterization of Coplanar Transmission Structures," to be published in the *Proceedings of IEEE LEOS '92 Annual Meeting—Symposium on Applied Optical Diagnostics of Semiconductor Materials and Devices,* Boston, MA, 16–19 November 1992.

J. M. Soures, R. L. McCrory, T. R. Boehly, R. S. Craxton, S. D. Jacobs, J. H. Kelly, T. J. Kessler, J. P. Knauer, R. L. Kremens, S. A. Kumpan, S. A. Letzring, W. D. Seka, R. W. Short, M. D. Skeldon, S. Skupsky, and C. P. Verdon, "The OMEGA Upgrade Laser for Direct-Drive Target Experiments," to be published in *Lasers and Particle Beams.*

J. M. Soures, "Solid State Lasers," to be published in *Nuclear Fusion by Inertial Confinement,* edited by G. Velerade, Y. Ronen, and J. M. Martinez-Val.

J. M. Soures, "High-Technology Advances from LLE Research," to be published in the *Rochester Business Profiles Journal.*

J. M. Soures, "The OMEGA Upgrade Laser Facility for Direct-Drive Experiments," to be published in the *Proceedings of the Fusion Power Associates Annual Meeting and Symposium,* Princeton, NJ, 25–26 June 1991, and in the *Journal of Fusion Energy.*

J. Sweetser, T. J. Dunn, I. A. Walmsley, C. Radzewicz, S. Palese, and R. J. D. Miller, "Characterization of an FM Mode-Locked Nd:YLF Laser Synchronized with a Passively Mode-Locked Dye Laser," to be published in the *Journal of the Optical Society of America B.*

C. J. Twomey, S. H. Chen, T. Blanton, A. W. Schmid, and K. L. Marshall, "Solid Polymers Doped with Rare Earth Metal Salts. II. Thermal Behavior and Morphology of the Neodymium Acetate-Poly(ethylene oxide) System," to be published in *Journal of Polymer Science, Polymer Physics Edition.*

R. Vanderhaghen, P. M. Fauchet, A. Mourchid, and D. Hulin, "The Cooling Rate of Hot Carriers in Disordered Semiconductors," to be published in the *Proceedings of QELS '92,* Anaheim, CA, 10–15 May 1992.

M. D. Wittman, R. Q. Gram, H. Kim, C. K. Immesoete, S. G. Noyes, and S. Scarantino, "Increased Retention Time for Hydrogen and Other Gases by Polymer Shells Using Optically Transparent Aluminum Layers," to be published in the *Proceedings of the 39th AVS National Symposium and Topical Conferences*, Chicago, IL, 9–13 November 1992.

W. Xiong, W. Kula, R. Sobolewski, and J. R. Gavaler, "Superconducting Properties of Laser-Annealed Lines Fabricated in Oxygen-Deficient Y-Ba-Cu-O Thin Films," to be published in the *Proceedings of the 6th Annual Conference on Superconductivity and Applications*, Buffalo, NY, 15–17 September 1992.

L. X. Zheng, T. Gong, W. Xiong, W. Kula, R. Sobolewski, and P. M. Fauchet, "Femtosecond Optical Nonlinearities in $YBa_2Cu_3O_{7-x}$," to be published in the *Proceedings of SPIE's OE/LASE '93*, Los Angeles, CA, 16–23 January 1993.

Conference Presentations

T. J. Kessler, "Unity Diffraction Efficiency and Its Applications to Intense Laser-Matter Interactions," Symposium on the Interaction of Focused Electromagnetic Fields with Optical Disk Structures, Rochester, NY, 1–2 October 1992.

W. Xiong, W. Kula, and R. Sobolewski, "Laser Writing: A New Technique for High Temperature Y-Ba-Cu-O Thin Films," Annual Meeting of the Rochester Chapter of IEEE Electron Device Society, Rochester, NY, 4 November 1992.

J. C. Lambropoulos, S. D. Jacobs, S. J. Burns, and L. Shaw-Klein, "Effects of Anisotropy, Interfacial Thermal Resistance, Microstructure, and Film Thickness on the Thermal Conductivity of Dielectric Thin Films," ASME Winter Annual Meeting, Session on Significant Questions in Heat Transfer, Anaheim, CA, 8–13 November 1992.

The following presentations were made at the Thirty-Ninth AVS National Symposium and Topical Conference, Chicago, IL, 9–13 November 1992:

H. Kim, J. M. Soures, and P.-C. Cheng, "Confocal Microscopic Characterization of Laser-Fusion Target."

M. D. Wittman, R. Q. Gram, H. Kim, C. K. Immesoete, S. G. Noyes, and S. Scarantino, "Increased Retention Time for Hydrogen and Other Gases by Polymer Shells Using Optically Transparent Aluminum Layers."

R. Sobolewski, "Electro-Optic Time Domain Characterization of Coplanar Transmission Structures," IEEE LEOS '92 Annual Meeting—Symposium on Applied Optical Diagnostics of Semiconductor Materials and Devices, Boston, MA, 16–19 November 1992.

The following presentations were made at the Thirty-Fourth Annual Meeting of the American Physical Society, Division of Plasma Physics, Seattle, WA, 16–20 November 1992:

R. E. Bahr, W. Seka, R. S. Craxton, and A. Simon, "Stimulated Raman Scattering in Long-Scale-Length Plasma Experiments on OMEGA."

R. Betti, A. Simon, and C. P. Verdon, "Dynamic Stabilization of the Ablative Rayleigh-Taylor Instability."

T. R. Boehly, R. S. Craxton, R. J. Hutchison, J. H. Kelly, T. J. Kessler, S. A. Kumpan, S. A. Letzring, R. L. McCrory, S. F. B. Morse, W. Seka, S. Skupsky, J. M. Soures, and C. P. Verdon, "Progress on the Upgrade to the OMEGA Laser System."

D. K. Bradley, "Applications of High-Speed-Gated X-Ray Imaging for Laser-Driven Implosions" (invited paper).

R. S. Craxton, W. Seka, R. E. Bahr, and D. L. Montgomery, "Hydrodynamic Simulations of Long-Scale-Length Plasma Experiments on OMEGA."

J. A. Delettrez, W. Seka, and R. L. Keck, "A Strategy for Laser-Beam Power Balance on the OMEGA Upgrade."

E. M. Epperlein, R. W. Short, and A. Simon, "Damping of Ion-Acoustic Waves in the Presence of Electron-Ion Collisions."

R. Epstein, C. P. Verdon, J. Delettrez, D. K. Bradley, and B. Yaakobi, "Simulations of Spectral Signatures of Core-Shell Mixing in Laser-Driven Implosions."

P. A. Jaanimagi, D. K. Bradley, R. L. Kremens, M. A. Russotto, and C. P. Verdon, "Neutron Streak Camera Diagnostic for ICF Implosions."

R. L. Kremens and M. A. Russotto, "Nuclear Diagnostics for the OMEGA Upgrade."

J. S. Li, C. J. McKinstrie, and A. L. Gaeta, "Nonlinear Oscillations and Chaos in Backward Four-Wave Mixing."

F. J. Marshall, J. A. Delettrez, R. Epstein, C. P. Verdon, and B. Yaakobi, "Diagnosis of CD Shell Implosion by Continuum Absorption Spectroscopy."

P. W. McKenty, J. H. Kelly, and S. Skupsky, "Numerical Investigation of Self-Focusing of Broad Bandwidth Laser Light."

C. J. McKinstrie and R. E. Giacone, "The Angular Dependence of SBS in Homogeneous Plasma."

D. D. Meyerhofer, "Prepulse-Free, Short-Pulse, High-Intensity, Laser-Plasma Interactions" (invited paper).

M. A. Russotto and R. L. Kremens, "Monte Carlo Studies of Charged Particle and Neutron Spectra in Laser Fusion Experiments for the Determination of High Fuel Areal Densities."

W. Seka, R. E. Bahr, R. S. Craxton, R. W. Short, and A. Simon, "Two-Plasmon-Decay Instability in Long-Scale-Length Laser Plasmas."

R. W. Short, and E. M. Epperlein, "Parametric Instabilities Driven by Inverse Bremsstrahlung in Laser-Produced Plasmas."

A. Simon, E. M. Epperlein, and R. W. Short, "The Effect of Weak Electron-Ion Collisions on Ion-Sound Wave Decay."

B. Soom, H. Chen, B. Yaakobi, and D. D. Meyerhofer, "K_α Emission from High-Contrast, Picosecond Laser-Plasma Interactions."

S. Uchida, H. Chen, Y.-H. Chuang, J. A. Delettrez, and D. D. Meyerhofer, "Characteristics of the Enhanced Field in High-Intensity Contrast Picosecond Laser-Produced Plasmas."

M. Yu and C. J. McKinstrie, "The Impulse Response of a Modulationally Unstable Wave."

The following presentations were made at the Optical Fabrication and Testing Workshop, Boston, MA, 17–19 November 1992:

M. J. Cumbo, A. Lindquist, and S. D. Jacobs, "Assessment of Frictional Forces in Optical Polishing Using Atomic Force Microscopy."

S. D. Jacobs, K. Kubath, and A. Maltsev, "Optical Fabrication Laboratory: Introductory Training for Optical Engineering Students."

J. Lambropoulos, M. J. Cumbo, and S. D. Jacobs, "The Effects of Material Properties and Process Parameters on Surface Quality during Microgrinding of Glass."

A. Lindquist, B. Puchebner, M. J. Cumbo, T. Rich, and S. D. Jacobs, "Bound Abrasive Polisher Concepts for the Center for Optics Manufacturing CNC Machining Centers."

W. E. Smith, T.-H. Bui, A. Lindquist, and S. D. Jacobs, "Non-Destructive Estimation of Subsurface Glass Damage Using Fluorescent Confocal Microscopy."

H. E. Elsayed-Ali, J. W. Herman, and E. A. Murphy, "Ultrafast Laser Superheating of Metal Surfaces," 1992 Materials Research Society Fall Meeting, Boston, MA, 30 November–4 December 1992.

J. H. Kelly, M. J. Shoup, III, M. M. Tedrow, and K. A. Thorp, "Design and Performance of a Modern, 15-cm-Aperture Brewster-Disk Amplifier," Lasers '92 (the Fifteenth International Conference on Lasers and Applications), Houston, TX, 7–11 December 1992.

ACKNOWLEDGMENT

The work described in this volume includes current research at the Laboratory for Laser Energetics, which is supported by New York State Energy Research and Development Authority, the University of Rochester, the U.S. Department of Energy Office of Inertial Confinement Fusion under Cooperative Agreement No. DE-FC03-92SF19460, and other agencies.

UNIVERSITY OF
ROCHESTER